Dynamic Plasticity Systems Direct Early Adaptation to Treatment in Neuroblastoma

Authors

Cecilia Roux[1,*], Sian Hamer[1,*], Abigail Shea[1,*], Emilia Chen[1], Ayeh Sadat Sadr[1], Christie English[1], Sarthak Sahoo[2], Alejandro Allo Anido[1], Harvey Che[3], Louis Chesler[3], Mohit Kumar Jolly[2], Michael David Morgan[4] and Alejandra Bruna[1].

[1]Centre for Evolution and Cancer, Division of Molecular Pathology, The Institute of Cancer Research, Sutton, United Kingdom

[2]Department of Bioengineering, Indian Institute of Science, Bangalore, India

[3]Division of Clinical Studies, The Institute of Cancer Research, Sutton, United Kingdom

[4]Institute of Medical Sciences, School of Medicine, Medical Sciences and Nutrition, University of Aberdeen, Scotland, United Kingdom

[*]C.R., S.H. and A.S. equally contributed to this work

A.B. corresponding author

Abstract

In paediatric cancers like neuroblastoma, limited genetic diversity emphasizes the role of phenotypic heterogeneity in driving malignancy. We investigated this phenomenon using experimental evolution and single-cell techniques in neuroblastoma preclinical models. Our findings reveal that neuroblastoma cells navigate multistable phenotypic landscapes, named plasticity systems. These finely regulate their topology and dynamics enabling tolerance, persistence, and regrowth in response to treatment. While preferential killing of adrenergic cells (ADRN), notably under cisplatin treatment, enriches drug-tolerant persister (DTP) populations with mesenchymal (MES) properties, we also observed phenotypic transitions contributing to DTP entry and exit. Additionally, single-cell-derived clone experiments unveiled a spectrum of heritable plasticity traits linked to functional properties, influencing DTP behaviour. Mathematical modelling supports the critical role of all cell phenotypes in evolutionary adaptation. Collectively, our study depicts plasticity systems as key early cancer drivers of adaptive evolution in neuroblastoma through regulating the multistability and dynamics of phenotypic landscapes. These insights underscore the necessity of decoding plasticity for advancing long-term therapeutic effectiveness.

Introduction

Neuroblastoma is the most common extracranial solid tumour in children typically less than 5 years old, and accounts for 15% of paediatric cancer mortality. Neuroblastoma is a malignancy of the developing sympathetic nervous system, mostly develops in the adrenal gland and occasionally originates from sympathetic ganglia

along the paravertebral sympathetic chains. One of the hallmarks of neuroblastoma is its wide range of clinical presentations and outcomes ranging from spontaneous remission to incurable disease. High-risk neuroblastoma is treated with multimodal high doses of therapy which is accompanied by long-lasting side effects that can be life-threatening. Yet around 50% of high-risk patients succumb to the disease due to recurrence and scarce treatment options[1]. This highlights the need to focus our efforts on understanding the mechanisms of relapse and the development of more manageable therapies.

Paediatric cancers have relatively quiet genomes, contrary to adult solid tumours which are frequently characterized by large-scale, extensive and recurrent chromosomal aberrations[2,3]. Recent studies show that key genomic events in childhood cancer include mutations or fusion oncoproteins that result in broad epigenetic changes[4]. Several genomic aberrations have been linked to high-risk neuroblastoma including amplification of *NMYC*, complex structural variations that result in the inactivation of *TERT* or deletions of *ATRX*, activating *ALK* mutations and alterations in the Ras pathway[5–8]. Comprehensive genomic profiling of neuroblastoma samples at diagnosis, and in relapse, has shown evidence of continued or parallel acquisition of structural variants constrained to the known neuroblastoma genomic driver loci (i.e., *MYCN*, *TERT*, *ATRX* and *MDM2-CDK4*) followed by convergent evolution of mutations targeting a few shared pathways[9]. The lack of consistent novel genetic events featured in relapse highlights that the genetic profiling of neuroblastoma might have reached its limits in providing comprehensive insights into the mechanisms driving relapse and treatment resistance.

On this basis, we hypothesize that phenotypic heterogeneity is instead a major driver of malignancy in paediatric cancers. Phenotypic heterogeneity could be attributed to distinct cells of origin and/or to the ability of cancer cells to transition between cell states, indicating a role for plasticity.

Recent single-cell RNA sequencing (scRNA-seq) studies of human embryonic and foetal adrenal medulla were performed to unravel neuroblastoma's transcriptional heterogeneity[10–15]. Discordant conclusions from these experiments highlight the complexity of scRNA-seq data analysis across multiple sample types and centres. One study used machine learning to derive a universal scRNA-seq map of neuroblastoma. Significantly, this unsupervised approach challenged the conventional notion of a singular neuroblastoma cell of origin[16] and highlights the unanswered question over the source of the observed heterogeneity in neuroblastoma. Moreover, it raises the question regarding the role plasticity plays in response to treatment, i.e. adaptive phenotypic plasticity.

To understand this phenomenon, we need biological models of neuroblastoma with heterogeneity that mimics that observed in patients, single-cell technologies with temporal resolution, and functional read-outs to discern sporadic transcriptional fluctuations from evolutionary phenotypic transitions. Neuroblastoma preclinical models including cell lines, genetically engineered mouse models and patients-derived tumour xenografts (PDXs) exhibit phenotypic heterogeneity[17,18]. The best-characterised phenotypes of neuroblastoma cell states are known as (nor-) adrenergic (ADRN) and mesenchymal (MES)/neural crest-like (NCC-like). These are defined by transcriptional and epigenetic profiles. ADRN and MES cell states can also be identified by cell surface

markers. Initial experiments identified plasticity, transitioning from ADRN to undifferentiated and resistant MES phenotypes during therapy *in vitro*. Significantly, while the presence of MES-like gene signatures has been reported in a minor subset of peripheral neuroblastic tumours and PDX mouse models[19,20], recent data show the ADRN profile is predominant in metastatic neuroblastoma[21]. Further studies are therefore needed to decode phenotypic transition types and principles, and investigate their evolutionary relevance.

In this study, we have pioneered a comprehensive framework that integrates methodologies from evolution with multiomics and single-cell barcoding techniques in a dynamic preclinical experimental model of therapy responses. Specifically, we induced drug-tolerant persister (DTP) cell populations in neuroblastoma preclinical models which represent the early stages of adaptive evolution[22–24]. These seemingly arrested cell populations regained proliferative capabilities upon treatment removal and gained a resistant drug profile. Our investigation reveals that treatment-specific phenotypic population changes occur through both plasticity-independent and plasticity-dependent evolutionary pathways. Plasticity, which we conclude is a key mediator, enables adaptive evolution in neuroblastoma by modulating phenotypic changes encompassing cell states with diverse degrees of commitment, dynamics, and functions. Significantly, plasticity is not uniformly distributed in neuroblastoma populations; it exhibits heterogeneity and heritability, undergoing natural selection under treatment conditions. In conclusion, our comprehensive study highlights the intricate interplay between phenotypic heterogeneity and adaptive evolution in response to treatment.

Results

Phenotypic Population Dynamics are Treatment-Specific

Preclinical models have demonstrated that post-treatment neuroblastoma samples are enriched in cells exhibiting a MES phenotype, which are known to be more resistant to conventional chemotherapy[17]. However, relapsed and metastatic patient samples, in the majority of cases retain their phenotypic features which are typically enriched in ADRN states[21]. This suggests a gap in our knowledge of the relationship between these two neuroblastoma states and their interaction with chemotherapy response. To address this, we explored the phenotypic dynamics within neuroblastoma cell populations after treatment.

Our primary focus was on the SK-N-SH cell line, well-known for its significant phenotypic heterogeneity, encompassing at least two well-characterized cell states: ADRN and MES[25]. We also identified and studied a further distinct cell state, referred to as hybrid (HYB), which displays a transcriptional profile that shares features of both ADRN and MES cells[26].

Before investigating the interplay with treatment, we asked whether these cell states had intrinsic plastic capability. We employed CD44 antibody-based fluorescence-activated cell sorting (FACS) to isolate ADRN ($CD44^{low}$), HYB ($CD44^{int}$) and MES ($CD44^{high}$) (Extended Data Fig. 1a). Phenotypic quantification of the resulting cell populations at different time points revealed state transitions in all conditions, albeit with varying dynamics (Fig. 1a and Extended Data Fig. 1a). Notably, HYB-enriched populations exhibited a tenfold

transition rate to MES state by day 2. ADRN-enriched populations quickly transitioned to HYB and MES states, resulting in a population structure comprising approximately 50% ADRN cells by day 12 (Fig. 1b). In contrast, MES-enriched populations exhibited slower transitions to other cell states, resulting in a population that remained 80% enriched in MES by day 12. These findings collectively demonstrated that all cell states possess plastic capabilities, each with varying degrees of dynamics. Additionally, we observed morphological and functional differences among cell states (Extended Data Fig. 1). For instance, ADRN cells replicated faster, HYB exhibited the highest colony-forming capabilities and MES had greater resistance to standard chemotherapies, consistent with prior observations[17] (Fig. 1c-d, Extended Data Fig. 1d, Extended Data Fig. 2a-d).

To address whether the frequency of cell states in the population could be influenced by treatment, we evaluated the effect on the cell state composition at different time points following exposure to 13 compounds. These included standard-of-care chemotherapies, targeted treatments, epi-drugs, and cell signalling modulators (Table 1). We observed treatment-specific population phenotypic changes (Fig. 1e and Extended Data Fig. 2e). After cisplatin treatment, a minority of cells persisted and were enriched in MES cell state after drug removal. Conversely, the EZH2 inhibitor Tazemetostat induced a persister cell population enriched for ADRN cell state under similar conditions (Fig. 1e, Extended Data Fig. 2a-b, and Supplementary Fig. 1-2). To our surprise, other epigenetic drugs, such as the Brd4 inhibitor JQ1, showed no changes in the cell state phenotypic population structure.

Overall, our data shows that treatment alters the phenotypic composition of neuroblastoma cells. However, these observations could be explained by either the selective killing of subpopulations or by inducing plastic cell state transitions.

Intrinsic Determinism Underlies Persistence in Neuroblastoma

To investigate the mechanisms underlying phenotypic changes in response to treatment, including the roles of plasticity and selective cell state killing, we utilized a barcoding approach within our dynamic preclinical drug response framework (Fig. 2a and Method). We selected two agents with different impacts on the phenotypic population structure: cisplatin, a DNA-damaging chemotherapy drug, and JQ1, an epigenetic drug known for inducing transcriptional reprogramming. Cisplatin significantly influenced cell state changes at the population level, while JQ1 had minimal impact on the overall clonal structure similar to what we had observed at the phenotypic level (Extended Data Fig. 3a and Fig. 1e).

Barcode sequencing unveiled a diverse repertoire of clones in each original population (POT) replicate. Among the potential 10,000 barcodes, a mean of 1437 unique barcodes were detected across POT replicates (Extended Data Fig. 3b and Methods). Notably, despite a fraction of the POT having been used for DNA sequencing, around 30% of these barcodes were shared between treatment naïve replicates. We denote barcodes that are present in independent replicate sister clones, indicating pre-existing proliferation and survival dominance (Extended Data Fig. 3c). In response to treatment, we noted clonal structures across all samples similar to that in

the POT, including independent replicates, suggesting that a degree of intrinsic determinism governs clonal dynamics, regardless of treatment (Extended Data Fig. 3c). Additionally, a mean clonal reduction of 35.14% occurred during cisplatin treatment and further decreased after cisplatin removal with a mean clonal reduction of 47.2% (Extended Data Fig. 3d).

To gain a better understanding of clonal dynamics in our pre-clinical neuroblastoma model, we calculated the Shannon Diversity Index[27] and clone frequency distribution. Our analysis confirmed a significant reduction in clonal diversity during and after removal of cisplatin treatment compared to untreated cells, as demonstrated by a significant reduction in Shannon diversity and shift of population in clone frequency distribution (Fig. 2b,c). The clonal structure of cisplatin deviated from the treatment naïve and POT barcode composition, while that on the JQ1 treated samples remained stable (Fig. 2c and Extended Data Fig. 3b-d). Examples of treatment-specific sister clonal dynamics, particularly those selected by cisplatin, are illustrated in Fig 2 (Fig. 2d,e and Extended Data Fig. 3e). For example, a clone in the POT (with clonal frequency of ~50) (Fig. 2e, far left column) was almost completely extinct following only 48 hours of cisplatin treatment. In contrast, the same barcode returned to a similar frequency after JQ1 removal (clone frequency ~25 ON-treatment vs. clone frequency ~50 OFF-treatment).

These observations collectively provide valuable information about clonal behaviour under different treatment conditions. They strongly suggest that under the influence of therapeutic pressure, clonal dynamics are primarily deterministic and thus predictable, epitomised by the observed dynamics in response to cisplatin treatment.

Transcriptional Shifts Occur During Dynamic Drug Response Processes

We next sought to relate our observed clonal dynamics with high resolution transcriptome profiling using single-cell RNA-sequencing (scRNA-seq; Fig. 3a). Our transcriptomic data obtained on 24,256 high-quality single cells across all experimental conditions (Fig. 2), unveiled the presence of nine distinct clusters. Each cluster was functionally annotated based on pathway analysis and cluster gene expression enrichment, and are hereafter referred to as cellular states 0-8 (Fig. 3a, Extended Data Fig. 3e and Supplementary Data).

As expected, we observed significant transcriptomic shifts among neuroblastoma clones enriched in signatures associated with critical biological processes linked to treatment's specific mechanism of action. For instance, cisplatin induced a shift towards a transcriptional state marked by an abundance of signatures associated with apoptosis, DNA damage response, and p53-activated genes. Notable genes in this context include *CDKN1A*, *FDXR*, *PHLDA3*, and *TP53I3*, which are predominantly found in cell cluster 4. Concurrently, we observed a decrease in signatures associated with cycling ADRN-like cells, exemplified by genes like *DLK1*, *CHGA/B*, *DBH*, *PHOX2A/B*, *GATA2/3*, and *CD24*, predominantly located in cell cluster 2 (Supplementary Information and Fig. 3b). On the other hand, JQ1 treatment induced a strong transcriptional state enriched in genes involved in chromatin remodelling. This pattern was exemplified by genes like *H2BC5*, *BRD2*, *H1-2*, and *H4C8*, primarily found in cell cluster 3. A similar signature was also induced in a small subset of ADRN-like cells (cell cluster 8), suggesting JQ1 affected both cell states (Fig. 3b).

Crucially, following the withdrawal of cisplatin, cells continued to shift their transcriptomic landscape towards cell states enriched in MES features (Fig. 3b). Upon the removal of JQ1 however, the transcriptional landscape of persister neuroblastoma clones rapidly reverted to a transcriptional profile resembling that of treatment-naïve populations. This transition encompassed cycling ADRN-like, cycling MES-like, and epithelial-mesenchymal transition (EMT) cellular state clusters.

To explore cell state changes during this dynamic treatment framework, we categorised each cell as either ADRN or MES using a marker gene set as a reference[25] (Extended Data Fig. 3f). We also statistically classified an intermediate hybrid cell category (HYB) based on a previously defined signature[28,29] (Extended Data Fig. 3g). Our findings, in line with the transcriptomic analysis, revealed a significant decrease in ADRN, both during cisplatin treatment and post-drug removal (Fig. 3c-e). Conversely, JQ1 treatment led to a loss of ADRN cells that rapidly reverted to an ADRN/MES population similar to the untreated condition after treatment removal (Fig. 3d,e).

To validate and extend these findings, we conducted experiments using patient-derived preclinical models within a similar dynamic drug response framework. We utilized NB039 and NB067 organoids, derived from *NMYC* amplified paediatric neuroblastoma patients with wild-type and mutant ALK, respectively[30]. Remarkably, the dynamics of responses to cisplatin and JQ1 in these patient-derived models at the RNA space closely mirrored those observed in our experiments with cell line-derived models (Extended Data Fig. 4). This reinforced the concept of common treatment-specific transcriptomic changes and, notably, confirmed the different cell phenotypic state population dynamics under cisplatin and JQ1 treatment schedules in both cell lines and patient-derived neuroblastoma preclinical models.

Plasticity and Selective Cell State Killing Coordinate Drug Tolerance, Persistence, and Regrowth

To further investigate chemotherapy response and cell state plasticity dynamics, we extended our analysis to a longer treatment follow-up period. We isolated SK-N-SH neuroblastoma cells via FACS, based on CD44 expression and treated them with either cisplatin or JQ1 as previously (Fig. 3f and Supplementary Fig. 3). Notably, there were no surviving ADRN cells after cisplatin treatment, and no regrowth was evident one week or one month after the removal of cisplatin (Fig. 3g, left panel). In contrast, surviving MES cisplatin-treated cells persisted treatment and slowly regrew after drug removal, repopulating the initial heterogeneous phenotypic population structure within one month. (Fig. 3g). This experiment demonstrated that cisplatin-induced persister cells are exclusively composed of MES cells, and these MES-like cells transition to ADRN cell states through MES-to-ADRN transitions (MAT) upon drug removal (Fig. 3g, right panel). Gene-set enrichment analysis conducted on RNA-seq data, along with functional assays assessing cell proliferation and senescence, provided confirmation that the surviving persister MES cells were in an arrested state after cisplatin treatment, which was completely reversed one month after cisplatin removal (Extended Data Fig. 5 and Extended Data Fig. 6a-c). Furthermore, MES-sorted cells that survived and persisted cisplatin treatment exhibited increased tolerance to cisplatin compared to untreated cells (Extended Data Fig. 6d, left panel).

Interestingly, upon repopulation, the cell culture regained cisplatin sensitivity comparable to the untreated originating culture (Extended Data Fig. 6d, right panel). Consequently, these functional characteristics led us to name the remaining cells after treatment as drug-tolerant persisters (DTP) cells. In stark contrast, we observed that JQ1 had no preferential killing of a particular cell state (Extended Data Fig. 2a and Extended Data Fig. 5). This is consistent with the previously observed stable phenotypic population structure throughout treatment (Fig. 1e). Importantly, both sorted ADRN and MES cells surviving and persisting JQ1 treatment retained plastic capabilities when treatment was removed (Fig. 3g, left panel).

In summary, our observations reveal that cisplatin treatment selectively targets ADRN cells, significantly contributing to the entry into a cisplatin-induced MES-only DTP state. However, under JQ1 treatment, there is no preferential killing based on cell state. Importantly, our evidence show both ADRN and MES cells retained their plastic capabilities during the treatment schedule and suggest plasticity is the key process that drives DTP exit and subsequent regrowth. To rule out the possibility that the observed findings were due to impure cell sorting, we employed the barcode DNA and RNA information to conclusively prove plasticity dynamics within our neuroblastoma model.

Cell State Alone Does Not Solely Determine Clonal Dominance

Initially, we hypothesized that the substantial selective killing of ADRN cells in response to cisplatin might indicate that cell state is the primary intrinsic determinant of clonal dominance (Fig. 2). To interrogate whether cell state predicts persistence, we assigned transcriptomic information to single cell barcoded clones. Surprisingly, within treatment-naïve populations, an average of 5.4% of clones were annotated to 3 cell states, 16.4% to 2, and 78.2% to 1 (Extended Data Fig. 7a,b). This suggests that at least 21.8% of neuroblastoma cellular clones undergo cell state switches either from ADRN to MES (AMT) or from MES to ADRN (MAT) during the barcode library expansion period. These transitions occur in the absence of any drug treatment, or apparent environmental stressors, therefore we incorporate them into our definition of plasticity. Moreover, the switching between cell states may constitute intrinsic plasticity in this system, and hence contribute to the population fitness. This interpretation may differ from other definitions of plasticity[31].

To uncover the relationships between phenotypic plasticity and DTPs, we analysed how clones which occupied a single cell state or cellular cluster persisted after treatment (Fig. 4a and Extended Data Fig. 7c,d). As expected, cisplatin DTPs were predominantly located in MES-like enriched clusters (clusters 5 and 7) (Fig. 4b). Tracing the pre-treatment transcriptomes of these clones revealed their origin primarily from MES-like enriched clusters (clusters 0, 1, and 5) (Fig. 4b). AMT cell state annotations further confirmed a higher frequency of MES cell states transitioning into a DTP during cisplatin treatment compared to the ADRNs (Fig. 4c). In contrast, assigning JQ1 DTP cell state annotations in pre-treatment revealed their origin from cells occupying ADRN and MES enriched clusters (MES: cluster 0, 1, and 5; ADRN: cluster 2) (Fig. 4d,e).

Despite MES being more likely to become DTPs, when visualising transcriptomic dynamic of cellular clones, we observed that a minor proportion of pre-existing ADRN-like cells (cluster 2 and ADRN cell state)

contributed to the MES-like cisplatin DTPs through AMT plasticity (Fig. 4f-h and Extended Data Fig. 7e-g). This analysis confirmed very few AMTs and MATs occurred during the treatment phase (Fig. 4f-h). However, these transitions increased in frequency during the OFF phase, particularly under JQ1 treatment, which returned to transition rates comparable to untreated conditions (Fig. 4f-h and Extended Data Fig. 7e-g).

Our observations show plasticity from ADRN to MES and MES to ADRN within treatment-naïve populations, as well as under treatment conditions. We observed a substantial impact of preferential killing of ADRN cells in response to cisplatin treatment, although evidence for a minor role of plasticity is present. However, exit from the DTP state and subsequent regrowth were predominantly mediated by plasticity (Fig. 4i). Given that neither cell state nor other transcriptional information alone was sufficient to predict future clonal dominance, we argue that plasticity may be the intrinsic determinant driving these dynamic processes.

Pseudotime Analysis Reveals Drug-Specific Adrenergic to Mesenchymal Transitions

The discrete nature of clustering methods prevents the assessment of cellular plasticity as a continuous process in scRNA-seq data. To address this, we employed trajectory analysis to assign pseudotime ordering to cells and relate this to an ADRN to MES continuum[32] (Extended Data Fig. 4c). This revealed multiple distinct trajectories within the inferred global lineage structure, indicative of treatment-specific AMTs (Fig. 5a and Extended Data Fig. 8a). Pseudotime progression and AMT score (low-to-high from ADRN-to-MES) were seen to be positively correlated, supporting that continuous transcriptional changes occur during AMT (Extended Data Fig. 8a, b).

We next aimed to identify candidate genes driving plastic responses to treatment by performing differential gene expression analysis along pseudotime. Genes that showed a statistically significant change along pseudotime represent potential molecular drivers involved in treatment adaptation and subsequent evolution. Most genes that decreased or increased in expression along pseudotime were archetypal ADRN or MES cell state markers, e.g. ADRN markers *DLK1* and *PHOX2A/B* decreased in expression, while MES genes *COL1A1*, *TPM1/2* and *ANXA2* increased in expression. While most of these potential plasticity driver genes were shared between ADRN to MES trajectories, treatment-specific drivers were also identified for JQ1 (e.g., *FTL*, *VIM*, *PRRX1*, *MT2A*) and cisplatin (e.g., *CAV1*, *CDK1A*) (Extended Data Fig. 8c-h and Supplementary Data).

In conclusion, our trajectory analysis highlights treatment-specific cell state transitions along an ADRN to MES continuum. Additionally, our identification of potential plasticity driver genes unveils distinct molecular pathways influencing adaptive responses under different therapeutic conditions.

Treatment Alters Plasticity Landscape Topology and Dynamics

We next aimed to further characterise the cell state transitions in the scRNA-seq data by modelling them as a multiscale switch process, an alternative to the entirely continuous perspective presumed by pseudotime analysis. We extended our analysis to dynamical manifold approaches, employing the multiscale method MuTrans to construct three-dimensional cell state landscapes[33] (Methods). Landscapes were inferred for each

treatment condition and showed distinct attractor states, which map to transcriptomic clusters but do not directly correspond to a single cluster (Fig. 5b-d and Extended Data Fig. 9a-f). Each well has a distinct gene expression profile that was characterised by gene set enrichment analysis (Supplementary Information, Extended Data Fig. 9g and Table 2). Notably, JQ1 and cisplatin landscapes exhibited a greater number of attractor wells, which increases the number of possible paths from one attractor state to another. The depth of each attractor well represents its potential transition 'energy', i.e. the deeper the well, the more 'energy' needed to transition out of it and hence higher stability. Across all conditions, MES-enriched states were frequently associated with deeper wells (higher stability) than ADRN-enriched states, supported by our observation of their lower transition rate (Fig. 1b). On the other hand, attractor wells associated with therapeutic stress and apoptotic phenotypes were typically shallower (lower stability) compared to other attractor wells, in the same landscape and of the same ADRN/MES state. For instance, in the cisplatin landscape the Stressed MES and Apoptotic MES wells had less negative potential energy values than the MES well, indicating that they are shallower and less stable (Table 2). These observations further support our findings of treatment-driven changes to cell state transitions.

To examine the dynamics of plasticity in the cell state landscapes, we characterised possible transition routes of AMTs and calculated transition probabilities between attractor wells. We first used maximum probability flow trees (MPFT) to map the global structure of transitions (Fig. 5e-g). Then we carried out transition path analysis for ADRN to MES transitions to infer transition probabilities (Fig. 5h-j). In the untreated condition, this revealed a major route of AMT via the cycling ADRN and cycling MES states (Fig. 5h). We also analysed the cisplatin-induced landscape, for which we calculated transition probabilities for three AMT paths, originating from the same ADRN-enriched state and each leading to a different MES-like state. All three analyses revealed multiple potential intermediate attractor wells, with the most probable routes proceeding via two MES attractor wells enriched for EMT signatures (Fig. 5i). In contrast, the two AMT path analyses inferred in the JQ1 condition mirrored that observed in the untreated condition (Fig. 5j). The prevalence of indirect routes, especially those via attractor wells enriched for EMT and cycling signatures, emphasises the role of intermediates in ADRN to MES cell state transitions.

These findings underscore the impact of treatments on plasticity landscape topology and dynamics, crucial for understanding adaptive responses and regrowth mechanisms. Nonetheless, we hypothesize that important plasticity traits may require further exploration.

Plasticity is a Heterogeneous and Hereditary Dynamic Trait

We next sought to gain a deeper understanding of the consequences of plasticity, its diversity within the neuroblastoma population and its hereditary nature using evolutionary approaches. We adapted Luria and Delbruck's fluctuation analysis, incorporating evolutionary principles of reaction norms to shed light on the subject.

We first isolated a pure population of ADRN cells from parental SK-N-SH cells and employed the Luria-Delbruck experimental framework to probe whether plasticity traits were predetermined by the originating

cell[34]. Notably, attempts to expand isolated MES cells proved challenging, potentially due to their lower proliferative capacities or the absence of necessary factors in this approach.

Our prediction was that if the ability of a population to display plasticity was determined by the originating cell, each population derived from a single cell would exhibit a unique phenotypic composition. Conversely, if all cells possessed uniform plasticity capabilities, the phenotypic compositions of these single cell-derived cultures would closely resemble each other (Fig. 6a). Analysis of phenotypic compositions conducted ten weeks after isolating single ADRN cells revealed a striking spectrum of plasticity traits in individual neuroblastoma clones (Fig. 6b). Notably, the majority of clones (15 out of 18) displayed a heterogeneous phenotype, featuring a mixture of ADRN and MES cells. In contrast, 3 out of 18 clones consisted of almost pure MES cells, signifying an early AMT with minimal or absent MAT plasticity traits. To underscore the heritability of these traits, a subset of clones was maintained in culture and analysed after several weeks, where their heterogeneous and pure MES compositions were consistently retained through passaging and cryopreservation (Extended Data Fig. 10a).

To validate that the observed phenotypic differences among clones were indeed attributable to variations in plasticity capacity, we employed a reactive norms approach (Fig. 6c)[35,36]. Rooted in evolutionary biology, reaction norms describe how and to what degree a phenotype (y) responds to changes in the environment (x). The slope of the reaction norm quantifies the degree of plasticity; a slope of zero indicates no phenotypic change across different environments, and a nonzero slope signifies a plastic response. We therefore assessed reaction norms within the framework of dynamic treatment responses. Eleven single-cell-derived clones and parental SK-N-SH cells were exposed to cisplatin for 7 days (environment 1), followed by immediate phenotype analysis by flow cytometry (CD44 expression). Upon removal of cisplatin and a subsequent 14-day culture in drug-free media (environment 2), we analysed the phenotypic composition by flow cytometry. In line with our prior observations, environment 1 exhibited an almost pure MES phenotype for all clones, affirming the preferential elimination of ADRN cells by cisplatin. Conversely, environment 2, representing drug withdrawal, yielded mixed ADRN/MES populations in parental SK-N-SH cells (Fig. 6d) and a reaction norms slope of 3.0. Remarkably, single-clone-derived cell populations demonstrated varying plasticity responses upon drug withdrawal. In environment 2, some clones displayed mixed ADRN/MES compositions, e.g. clones P, Q and O, which exhibited reaction norms slopes of 2.8, 1.1 and 0.8 respectively. Conversely, others maintained pure MES states, e.g. clones A, B, C, all with reaction norms slopes of 0.0. These reaction norms illustrated both the existence of a continuous spectrum of plasticity traits, and the ability to quantify their intensity across treatment conditions (Fig. 6d and Extended Data Figure 10b).

To explore whether the observed variability in plasticity traits could be explained by genetic alterations, we selected ten of the single cell-derived clones for genomic analysis (Supplementary Figure 4-5). Clones were categorised into two groups (plastic or fixed) representing their intrinsic plasticity trait, based on their phenotypic composition and their reaction norms slope. Strikingly, clones were characterized by a unique composition of mutations; however, unsupervised clustering of mutational variant allele frequency (VAF) failed to separate clones by their plasticity trait. In addition, we failed to identify any mutations or copy number

aberrations (CNA) unique to either plasticity trait group. While we cannot exclude the possibility that individual clones possess genomic alterations that may confer/constrain plasticity, these data show that plasticity is an intrinsic, heritable trait occurring at heterogeneous levels with no common root in the DNA sequence of exomes.

Functional assessments of the single-clone-derived cultures unveiled significant disparities in growth rates and cisplatin sensitivity (Fig. 7a, Extended Data Fig. 10c-d). Clones with pure MES populations exhibited slower proliferation rates and lower responses to cisplatin, consistent with the characteristics of FACS-sorted MES cells (Extended Data Fig 1d and Extended Data Fig. 2a). In contrast, clones with heightened plasticity traits displayed increased proliferation rates and greater responsiveness to cisplatin treatment.

Given our observation that plasticity occurs as a heterogeneous trait within cell populations, we reasoned that this trait could itself be selected for (or against) during environmental pressure. We used mathematical modelling to further investigate the principles governing clonal and transcriptional dynamics under cisplatin treatment. The model is a system of differential equations capturing interactions among various cell phenotypes within a heterogeneous population. It represents the temporal evolution of four phenotypes (ADRN plastic, ADRN fix, MES plastic, and MES fix), assuming an initial composition akin to parental SK-N-SH cells (Fig. 7b). Simulations start with randomly sampled parameter values, exploring diverse configurations allowed by the population of cell states. Growth rates and transition rates between phenotypes, reflecting ADRN and MES traits, were sampled based on defined experimental bounds (Supplementary Fig. 6 and Methods). The model revealed that, in the presence of cisplatin, the total population size was smaller than in untreated populations (Fig. 7c), with an enrichment of MES phenotype fitting the observed cisplatin-induced MES DTP populations (Fig. 7d,e and Fig. 1e and Fig. 3). This suggests MES cells persist and proliferate even in the presence of the drug. Significantly, a subset of ADRN phenotype was also enriched, consistent with experimental findings. Crucially, the model also predicts the enrichment of plastic ADRN and MES cell subpopulations after cisplatin, indicating positive selection for highly dynamic plastic cell states (Fig. 7f,g) supporting our hypothesis. In summary, our modelling supports that ADRN states contribute to the emergence of a MES-DTP population post-cisplatin, and suggests that highly dynamic and plastic systems are enriched through treatment regimes.

In conclusion, our study introduces the ground-breaking concept that plasticity is a trait characterized by both heterogeneity and heritability. We propose that plasticity serves as an evolutionary strategy in high-risk neuroblastoma, preparing cells to adapt to various environmental changes (Fig. 7h). Additionally, plasticity is enriched under environmental pressure. This conceptual model is supported by mathematical modelling, illuminating the fundamental role of plasticity systems - comprising both a process and a trait - in evolutionary adaptation. Taken together, our data suggests that targeting the plasticity systems could be a more effective therapeutic strategy than focusing on cell states to impede regrowth.

Discussion

Our study investigates the intricate relationship between phenotypic diversity, adaptive evolution, and treatment responses in neuroblastoma. Through a comprehensive framework that integrates classical evolutionary methods with advanced single-cell technologies, we gain insights into the dynamic responses to therapy. Based on evidence presented here, we redefine plasticity[31] as a biological system representing both a process and a trait. The former depicts the dynamics, topology and energy of the phenotypic landscape within populations, while the latter represents a heritable trait upon which selection can act.

Childhood cancers, marked by disrupted developmental processes, are thought to adapt and evolve by leveraging the embryonic ability to switch cell identities without genomic changes - a phenomenon known as cell plasticity[13,15,19]. Rooted in the plasticity-first evolution perspective[37,38], we hypothesized that the molecular mechanisms involved in phenotypic transitions during the early stages of adaptation to treatment could act as a cancer driver. However, studying plasticity has faced challenges due to technological limitations. For instance, approaches like scRNA-seq provide evidence of cellular phenotypic diversity but lack time resolution. In addition, scRNA-seq often falls short in identifying transient fluctuations from the transcriptional changes of biological meaning. The latter require some level of epigenetic memory to convey biological meaning and we hypothesise these underpin plasticity-first evolution[10–15,20,39–41]. Our study addresses these challenges through an in-depth exploration of the relationship between cell states and treatment effects by combining evolutionary experimental approaches with integrated DNA barcodes readable on DNA and scRNA-seq platforms. Here we shed light on the principles of plasticity-first evolution and point toward the potential role of plastic drivers and predictors of early adaptation and subsequent cancer evolution.

We observe population dynamics under various treatments, underscoring the evolutionary relevance of the heterogeneous phenotypic nature of high-risk neuroblastoma. Environmental pressure can lead to the enrichment of a HYB cell state, bridging characteristics between ADRN and MES cells. Crucially, all cell states demonstrated plastic capabilities, each with unique commitment and transition rates. The preferential killing of ADRN cell states in response to cisplatin treatment, coupled with evidence of low-frequency AMT events, contributes to MES-prevalent cisplatin-induced DTP populations. This highlights a minor role of plasticity in driving entry into DTP states, and demonstrates that both ADRN and MES cell states contribute to DTPs in response to treatment. In addition, plasticity reverts DTPs to a phenotypically diverse neuroblastoma population resembling the parental cells. The functional differences among cell states underscore the robust nature of plasticity systems, enabling cells not only to persist through treatment by transitioning to treatment-resistant states but also to repopulate and regrow by transitioning back to highly replicative states[17,40].

Trajectory analysis and dynamical manifold approaches provide a two- and three-dimensional perspective, respectively, on cell state landscapes. We observe intrinsic plasticity landscape topology and dynamics are shaped under therapeutic stress. MES-enriched attractor states typically showed higher stability consistent with their slower transition dynamics and higher phenotypic commitment, compared to the ADRN. Interestingly, shallower wells are linked to therapeutic stress and apoptotic phenotypes. These data depict the complex landscape of plasticity systems and highlight the presence of several intermediate routes contributing to the observed phenotypic heterogeneity.

Classical evolutionary approaches[34–36,42–44] revealed that plasticity behaviour at the population level is a consequence of a highly orchestrated system. This is rooted in the heterogeneous and heritable nature of plasticity traits in individual cells within the neuroblastoma population. These traits exist in the absence of any common genetic events linked to plasticity capacity, highlighting that the genomic coding region is unlikely to play a major role in underscoring this trait. Furthermore, mathematical modelling supported that plasticity, rather than cell state, is an intrinsic determinant driving dynamic drug response processes of early adaptation to treatment. Crucially, our data provides evidence that plasticity traits are positively selected upon environmental pressure.

In summary, our study suggests that neuroblastoma populations are pre-adapted to environmental changes through exhibiting heterogeneity of plasticity systems. This challenges the prevailing notion that a single cell state is the sole determinant of drug tolerance and persistence, highlighting the role of plasticity as a cancer driver. ADRN cells represent an equally fit state in the eyes of evolution, challenging the current focus on targeting the MES state. This conceptual shift has strong implications for therapeutic strategies, supporting the idea that targeting plasticity systems is more effective in impeding regrowth than solely focusing on MES and/or other drug-resistant cell states. This finding has the potential to influence the development of more targeted and successful treatment approaches for high-risk neuroblastoma with long-term benefits.

Methods

Cell lines and treatment

SH-EP, SH-SY5Y, SK-N-AS, SK-N-Be(2c) and SK-N-SH human neuroblastoma cells were cultured in DMEM (Thermo Fisher) supplemented with 10% fetal bovine serum (FBS) (Thermo Fisher), 100 IU penicillin and 100 μg/ ml streptomycin (Sigma). IMR32, Kelly, LAN5 human neuroblastoma cells were cultured in RPMI (Thermo Fisher) supplemented with 10% fetal bovine serum (FBS) (Thermo Fisher), 100 IU penicillin and 100 μg/ ml streptomycin (Sigma). All cell lines were originally provided by L. Chesler, ICR, London. For SK-N-SH assays compounds were administered at the following concentrations: 0.107 uM doxorubicin (Sigma), 3.18 uM cisplatin (Cambridge Bioscience), 10 uM lorlatinib (Cambridge Bioscience), 15 uM ruboxistaurin (Selleck Chemicals), 100 uM deferoxamine mesylate (Selleck Chemicals), 2 uM retinoic acid (Selleck Chemicals), 0.66 uM JQ1 (Selleck Chemicals), 1 uM tazemetostat (Selleck Chemicals), 45.59 uM IWP-2 (Cambridge Bioscience), 64.63 uM XAV-939 (Selleck Chemicals), 5 uM CHIR99021 (Selleck Chemicals), 10 uM TGF-β RI Kinase Inhibitor VI, SB431542 (Merck), 0.1 uM recombinant human TGF-beta 1 (Bio-Techne).

Patient-derived models and treatment

NB039 ($MYCN^{AMP}$ ALK^{WT}) and NB067 ($MYCN^{AMP}$ ALK^{R1275Q}) patient-derived cells (originally provided by J. Molenaar, Princess Maxima Centrum, Netherlands) were cultured in low-Glucose GlutaMAX DMEM (Thermo Fisher) supplemented with 25% Ham's F-12 Nutrient Mix, B-27 Supplement (50X) (Thermo Fisher), minus vitamin A N-2 Supplement (100X) (Thermo Fisher), 100 U/mL penicillin-streptomycin (Sigma), 20 ng/mL Animal-Free Recombinant Human EGF (Peprotech), 40 ng/mL Recombinant Human FGF-basic (Peprotech),

200 ng/mL Recombinant Human IGF-I (Peprotech), 10 ng/mL Recombinant Humand PDGF-AA (Peprotech) and 10 ng/mL Recombinant Human PDGF-BB (Peprotech). NB039 and NB067 cells were treated with the following concentrations: 2.27 uM cisplatin (Cambridge Bioscience) and 1 uM JQ1 (Selleck chemicals).

Flow cytometry and sorting

For antibody staining of cell surface molecules, isolated cells were aliquoted into 5mL polystyrene FACS tubes, and washed with 2 mL PBS supplemented with 1% BSA (referred to as FB buffer). Cells were pelleted at 400 g for 5 minutes at 4 °C, resuspended in 100 μL FB, and incubated for 30 minutes on ice with the following antibody: anti-CD44 APC/Fire 750 (1:100, Biolegend, 103061), anti-CD24 PE (1:20, eBioscience, SN3 A5-2H10). Stained cells were washed twice by centrifugation in 2 ml FB at 400g for 5 minutes at 4°C. Washed cells were resuspended in 25 ng/mL DAPI (Miltenyi), and analysed by flow cytometry (Symphony A5, BD Biosciences) or sorted by FACS (Symphony S6, BD Biosciences; SONY MA900 or SONY SH800, SONY) as above. The data were analysed with FlowJo software.

CFSE-based proliferation assay

Cells were labelled with 0.5uM CFSE (Invitrogen) following manufacturing instructions and incubated for a maximum of 12 days. CFSE dilution was measured by flow cytometry. The data were analysed with FlowJo software.

Immunofluorescence

For immunofluorescence staining, 2x 10^5 cells were seeded in a 24-well plate containing glass coverslips. The day after, cells were treated with either Cisplatin or JQ1 for the indicated amount of time. After treatment, cells were fixed with 4% PFA for 30 minutes at 4°C. Cells were then permeabilized with 0.2% Triton X-100 for 10 minutes at RT. Cells were washed twice and incubated in PBS buffer containing 1% BSA and 2% FCS (IFF buffer) for 30 minutes at room temperature (RT). Cells were stained overnight at 4 °C with primary antibody diluted in IFF buffer (anti-CD44 IM7, 1:500, eBioscience; anti-LGR5 OTI2A2, 1:200, Abcam; anti-GATA3 D13C9, 1:1000, Cell Signalling, anti-gH2A.XpPhospho (Ser139) 2F3, 1:200, Biolegend). The following day, cells were washed three times with PBS and subjected to conjugated secondary antibody diluted in IFF buffer (anti-Mouse-AF488 A21202 Invitrogen, anti-Rabbit-568 A11036 Invitrogen, anti-Rat-AF647 A78947 Invitrogen) at 1:2000 for 2h at RT. Coverslips were mounted with DAPI Fluoromount-G mounting medium and imaged the with a confocal microscope (Zeiss LSM700).

RT-PCR

RNA was isolated using the RNeasy Kit (Qiagen) and reverse transcribed using the RevertAid kit (Thermo Scientific) according to the manufacturers' instructions. Quantitative RT-PCR was performed using SYBR Green primers (Applied Biosystem). Human *Actin* and glyceraldehyde-3-phosphate dehydrogenase (*GAPDH)* were used as housekeeping genes to calculate relative mRNA expression. All mouse and human primer sequences are described in Table 3.

Beta-galactosidase staining

SA-β-gal was stained using the Senescence Associated β-Galactosidase Staining kit (Cell Signaling) at pH6, according to the manufacturer's protocol. Images reflect representative results of at least three independent experiments.

Dose response curves

Cell lines and neuroblastoma organoid cultures were seeded at 2000 cells/well and 5000 cells/well respectively in 384-well plates and cultured for 24 hours prior to dosing. Cells were dosed using Echo 550 liquid handler, using a 7-dose response curve per compound with three technical replicates per concentration. Cell viability was assessed using CellTiterGlo-3D (Promega,) or resazurin (final concentration 25 ug/mL, Abcam) as indicated in the main text. Cell viability was assessed at day 3 and day 7 after dosing for cell lines and neuroblastoma organoid cultures respectively, due to differential growth dynamics. Cell viability was normalised to background and solvent controls, and dose response curves were fitted using isotonic regression, as previously described[45].

Colony forming assay

For the colony forming assay cells were seeded at 1000 cells/well of a 6-well plate in complete media. Colony growth was monitored, and media was replenished once a week. Plates were fixed and stained with methanol and Giemsa once colonies reached sufficient size to be counted with the naked eye.

Barcoding of cell lines

The CloneTracker library was a gift from Andrea Sottariva (BCXP1M3RP-XSP, Cellecta). SK-N-SH cell lines were cultured in normal growth media and barcoded by lentiviral transduction according to manufacturer's recommendations. Following lentiviral titration, we transduced 1 million neuroblastoma cells using a lentiviral library using a multiplicity of infection (MOI) of 0.1 (corresponding to 10% of cells transduced) to attain a single barcode per cell. 10,000 barcoded cells were FACS-sorted based on RFP-positivity and expanded to approximately 100 times the barcode library representation, constituting the "original population" or POT.

Experimental design of Single cell RNA sequencing

The 0.1 million barcoded SK-N-SH cells were FACS-sorted in aliquots of 10000 cells and expanded prior to cryopreservation. Of these frozen cells, 4 million cells were thawed and again expanded to 60 million cells. These cells were seeded into 9 T175 flasks equally. Three flasks were treated with DMSO as control, three were exposed to cisplatin treatment (3.18 μM) and three to JQ1 treatment (0.66 μM). After 2 days, the treatment was removed and cells were detached, 10% of the total population was cryopreserved in two aliquots of 5% and the remaining cells were reseeded and grown under normal growth media for 1 week (JQ1) or 10 days (cisplatin). Cell counts were determined via the Countess II Automatic Cell Counter (Thermo Fisher).

Cellecta barcodes bioinformatics analysis

FASTQ files were mapped to a custom index reference generated from white-list (all possible sequences) of Cellecta barcodes, using Burrows-Wheeler aligner (BWA-MEM tool; version 0.7.17)[46]. Once mapped BAM files were generated using Sequence Alignmnet/Map (SamTools; v1.18)[47]. Gene counts were quantified using featureCounts from Rsubread.

To observe clonal dynamics, representative percentage was calculated for each clone within each sample (frequency of Cellecta barcode / frequency of all Cellecta barcodes x 100). Shannon diversity index[27] was calculated between conditions to observe changes in clone diversity as per following equation: $H=-\sum[(pi)\times log(pi)]$, where *pi* is proportion of individual clone within the population. Statistical significane of results was determined using pairwise t-tests and false discovery rate (FDR) < 0.05. Estimated clone frequency was calculated as number of cells present before NGS library preparation x frequency of barcode from sequencing.

Single cell RNA profiling

Single cells were prepared from untreated, cisplatin and JQ1 treated samples. After centrifugation, single cells were washed with PBS and were resuspended with a buffer (Ca++/Mg++ free PBS + 0.04% BSA). Cells were tagged with the CMO oligos (10X Genomics) as per manufacturer's instructions. Samples were multiplexed in groups of 6, each containing 5000 cells/samples for a total of 30000 cells/pool.

Pooled single cell suspensions were loaded on a Chromium Single Cell 3′ Chip (10X Genomics) and were run in the Chromium Controller to generate single-cell gel bead-in-emulsions using the 10X genomics 3′ Chromium v2.0 platform as per manufacturer's instructions. Single-cell RNA-seq and CMO libraries were prepared according to the manufacturer's protocol and the library quality was confirmed with a Bioanalyzer High-Sensitivity DNA Kit (Agilent, 5067-4627). Cellecta barcode libraries were prepared using 25% of the adaptor-ligated cDNA to amplify only the barcoded cDNA product. Barcodes were pre-amplified using the P5-Read1 primer (ACACTCTTTCCCTACACGACGCTCTTCCGATCT) and the P7-Adapter-FBPI Cellecta primer (GTGACTGGAGTTCAGACGTGTGCTCTTCCGATCTCCGACCACCGAACGCAACGCACGCA), following which Illumina indexes were added. Samples were sequenced on an Illumina NovaSeq 6000 according to standard 10X Genomics protocol, aiming for approximately 50,000 reads per cell for gene expression libraries and 1000 reads per cell for CMO/Cellecta barcode libraries.

Single cell data pre-processing

10x Genomics CellRanger (v6.1.2) was used to process raw sequencing FASTQs, using cellranger multi pipeline to conduct read alignment, sample demultiplexing and generate feature-barcode matrix. EmptyDrops method from DropletUtils (v1.20.0) package[39,48] was implemented on cellranger output H5 matrix to remove empty droplets with false discovery rate of 0.1%. Data files from each multiplexed pool were merged and then normalised using logNormCounts from scuttle (v1.10.1) package[49] for downstream QC and processing.

Cell-level filtering was carried out with the following thresholds: mitochondrial gene content <10%, ribosomal gene content >5%, and UMI counts >1000. Filtering at the gene-level was implemented to remove genes with fewer than five reads. Downstream normalisation and scaling were performed using Seurat (v4.3.0)[50] with the SCTransform function, using the top 1000 variable genes, and regressing out cell cycle and mitochondrial genes. Downstream normalisation and scaling were performed using Seurat (v4.3.0) with the SCTransform function, using the top 1000 variable genes, and regressing out the number of UMIs (by default), cell cycle and mitochondrial genes. The SCTransform data output was used to perform a principal component analysis (PCA). The batch correction algorithm Harmony (v0.1.1) was applied across CMO multiplexed pools, and the output used for Uniform Manifold Approximation and Projection (UMAP)-based dimensional reduction. Clustering was carried out using the Seurat FindClusters function and gene expression markers for the clusters were

identified by a Wilcoxon Rank Sum test, using the Seurat FindAllMarkers function. Gene set enrichment analysis using clusterProfiler (v4.6.2)[51,52] was then carried out on the cluster markers.

AMT score generation

Single-cell expression signatures for the ADRN and MES cell states were created using the AddModuleScore function in Seurat and published gene sets[18]. Two methods were used to calculate the AMT score: (1) the ADRN score was subtracted from the MES score for each cell, or (2) a scoring method based on that used by Tan et al.,[29]. The latter used statistical testing (*t*-tests) to determine whether differences between ADRN and MES gene set expression were significant. The *t*-statistic was taken as the AMT score and the statistical significance was further used to segregate cells into phenotypic groups: ADRN (AMT score < 0; $P < 0.05$), intermediate ADRN (AMT score < 0; $P \geq 0.05$), intermediate MES (AMT score > 0; $P \geq 0.05$) and MES (AMT score > 0; $P < 0.05$). The two intermediate classifications were grouped together as HYB.

DTP identification

Clones of interest (DTPs) were identified as those clones which appeared post-treatment and could be traced back through beginning of experimental window. Transcriptomic information was visualised using UMAP projection. Clonal information was linked to experimental replicate and associated to transcriptomic information using alluvial plot throughout experimental timeframe to track both AMT state and cellular cluster changes.

Trajectory inference

Trajectory inference was carried out using Slingshot (v2.6.0), which was run with the dimensionality reduced produced by PCA, cluster labels identified by Seurat FindClusters (resolution = 0.8) and setting the root to an ADRN cluster[32]. Gene dynamics analysis by fitting a linear spline model to each lineage was carried out using TSCAN (v.1.36.0). A random forest-based approach was also used for trajectory-based differential expression analysis. For each lineage, the expression data for the top 300 highly variable genes was randomly split (3:1) into a training and testing set, and a random forest regression was applied using the parsnip (v1.1.0) package.

MuTrans analysis

Pre-processing of the scRNA-seq data, split by drug condition, was carried out using Seurat, as outlined above. Analogous processing was carried out using Scanpy (v1.9.3)[50,53]. Using the filtered data as inputs, the count matrices were normalised and log transformed with a pseudo-count of 1. The number of transcripts per cell and the mitochondrial content were regressed out and the data was scaled, prior to PCA. Dimensionality reduction using UMAP and Leiden clustering was carried out. Cluster markers were then found using Wilcoxon rank-sum tests.

A neighbourhood graph was computed for the processed data using scanpy.pp.neighbors (metric = “cosine”). Construction of cell-fate dynamical manifolds and downstream analysis of cell-state transition was then performed using the MUltiscale method for TRANSient cells[33]. The attractor wells were annotated by marker finding using Seurat and gene set enrichment analysis using clusterProfiler, as well as by considering which annotated transcriptomic clusters they correspond to.

Cellecta barcodes amplification and next generation library preparation

SK-N-SH cells were harvested and pelleted at the relevant timepoints. Genomic DNA was isolated using AllPrep kit (Qiagen) according to manufacturer's instructions and quantified using Qubit (Life Technologies). Amplicon PCR was conducted using 50ng of DNA (or 20ng for samples with lower DNA yield) along with 2x Accuzyme mix (Bioline) to amplify barcodes using the following primer sequences (Forward - ACTGACTGCAGTCTGAGTCTGACAG, Reverse - CTAGCATAGAGTGCGTAGCTCTGCT). After identifying and purifying PCR product (consisting of 80-bp product + 30-bp semi-random barcode), NGS libraries were prepared using NEBnext Ultra II DNA library preparation kit for Illumina (New England Biolabs) and quantified with using a TapeStation (Agilent Genomics). Samples were balanced and pooled together to have final molarity of 4nM, NGS was then performed by ICR Genomics facility (TPU) using NovaSeq SP PE150.

Bulk RNA sequencing

RNA was isolated using AllPrep kit (Qiagen) according to manufacturer's instructions. RNA sequencing was performed by BGI Tech Solutions using Paired End reads 100 with DNBSEQ technology (30M reads/sample). The quality of raw reads data was assessed using FastQC (v0.11.9)[54]. After checking the quality parameters, the reads were aligned to the human reference genome (GRCh38/hg38) using the STAR aligner (v2.7.6a)[55]. Gene expression levels were quantified as raw read counts mapped to each gene using HTSeq (v0.12.4)[56]. We used a probabilistic method within the DESeq2 program[57], a Bioconductor software package that employs a negative binomial distribution to model RNA-seq count data, to evaluate the differential gene expression. The affected genes were determined based on a false discovery rate (FDR) < 0.05 and a log Fold change (FC) > 1.

To functionally interpret the list of differentially expressed genes, we performed Gene Ontology (GO) enrichment analysis. The analysis was conducted using the clusterProfiler (v3.17) package in R[51,52].

Single-cell derived clones generation

SK-N-SH cells were sorted into CD44-low (ADRN) and CD44-high (MES) populations by FACS. Sorted cells were seeded in 12-well plates (~50,000 cells/well) and cultured for 4 days. Cells were then reseeded in 96-well plates to generate single-cell cultures using limiting dilution approaches (seeding density of 0.5 cells/well), in 50% conditioned media and 50% fresh culture media. Fresh media was added to cells once per week, and each single cell clone was expanded for approximately 10 weeks. Single cell clones were then analysed by flow cytometry (as described above) to determine the proportion of ADRN and MES cells.

To generate conditioned media, SK-N-SH cells were seeded at low density and cultured for 5 days without refreshing the culture media. After 5 days, media was collected from culture flasks and centrifuged 250xg for 10 minutes. The top 90% of media was collected and filtered (0.22um) prior to use.

Genomic analysis of single cell-derived clones

Genomic DNA was isolated using AllPrep kit (Qiagen) according to manufacturer's instructions. Whole exome sequencing (WES) and shallow whole genome sequencing (WGS) was performed by BGI Tech Solutions. For WES, exome capture was performed using Agilent SureSelect V6 kit, and sequenced using Paired End 100 reads with DNBSEQ technology (50x depth). For WGS, libraries were sequenced using Paired End 100 reads with DNBSEQ technology (1x depth).

For both WES and WGS analysis, the quality of raw reads data was assessed using FastQC (v0.11.9) (https://www.bioinformatics.babraham.ac.uk/projects/fastqc/). After checking the quality parameters, the reads were aligned to the human reference genome (GRCh38/hg38) using the BWA-MEM tool[46] (Version 0.7.17), then duplicate reads were marked and removed using Picard tools (Version 2.23.8) (http://broadinstitute. github.io/picard). For WES, GATK[58] (Version 4.1.9.0) (Genome Analysis Toolkit) was used to perform Base Quality Score Recalibration, to adjust the quality scores of the sequencing reads, which increases the accuracy of the variant calls. MuTect2[59] was used to call variants. It's specifically designed for calling somatic variants in cancer samples, distinguishing them from germline variations. MuTect2 (included in GATK) was used to analyse the aligned reads, using the tumor mode to identify somatic mutations. This was also used to filter variants based on different criteria, reducing false positives. For WGS, to identify copy number alterations (CNAs), we used QDNAseq[60] v1.38.0 - an R package optimized for detecting CNAs.

Reaction norms and functional characterisation of single cell derived clones

Single cell clones and parental SK-N-SH cells were seeded at 200,000 cells/well in 2 mL of media in 6-well plates using 4 replicate wells per sample. 24 hr after plating, cells were dosed with cisplatin (3.18 uM). 7 days after dosing, 2 wells per sample were harvested and analysed by flow cytometry for CD44 expression (as described above). The remaining 2 wells per sample were washed once with PBS and 2 mL of fresh media was added. 14 days after drug withdrawal, 2 wells per sample were harvested and analysed by flow cytometry for CD44 expression (as described above). Fresh media was added once per week during the drug withdrawal phase.

Cisplatin drug responses and growth dynamics of the single cell clones and parental SK-N-SH cells were analysed in parallel with reaction norms. Cisplatin drug response was tested in two ways: dose response curve and response to a fixed concentration. The dose response curves were generated using the protocol described above using a 6-dose range of 2, 0.6, 0.2, 0.06, 0.02, 0.006 uM and cell viability was measured after 3 days using CTG-3D (Promega). To test the response to a fixed concentration of cisplatin 20,000 cells were seeded in a 12-well plate using 3 replicates per condition. 24 hr after plating, cells were dosed with 3.18 uM cisplatin (to match reaction norms) or left untreated. Cell viability was measured 7 days after dosing using resazurin (Abcam).

To assess growth dynamics, cells were seeded at 4000 cells/well in 200 uL of media in 96-well plates using 5 replicate wells per sample. Images were acquired using the Incucyte S3 at 10x magnification every 6 hours for 7 days. Percentage confluency was calculated based on surface area coverage using Incucyte (Sartorius) image analysis software.

Mathematical modelling for single cell derived clones growth dynamics

We used a system of two differential equations model the growth and transition dynamics between adrenergic (ADRN) and mesenchymal (MES) cell populations. We assumed that the growth of ADRN cells were twice that of the MES cells. We further assumed that the initial cell clone composition in our simulations was set to be the same proportions as that obtained from the flow cytometry characterisation of the single cell clones. Based on the available time course data, we estimated the growth rates of the ADRN and MES phenotypes and the transition rates between the ADRN and MES phenotypes. Parameters were estimated using the curve_fit

function which uses the Levenberg-Marquardt algorithm to minimize the residuals between each individual growth trajectory.

Mathematical modelling for Mesenchymal cell population enrichment under cisplatin treatment

The mathematical model employed in this study is a system of differential equations capturing the dynamic interactions among different cell phenotypes within a heterogeneous cell population. The model represents the temporal evolution of adrenergic (ADRN), mesenchymal (MES), and plastic (*) cell populations. Simulations are initiated with initial conditions and parameter values sampled randomly from a uniform distribution in the range [0,1]. Furthermore the range of the growth rate of the mesenchymal cells were set to be from 0 to 0.5 signifying the slower growth rates of MES phenotype and the death rate of MES cell phenotypes were also sampled from 0 to 0.5 to signify the slower kill rate of the MES phenotype cells due to the drug, cisplatin. The system of differential equations is numerically solved until a steady state is reached or the simulation time reaches 500, whichever occurs earlier. This model structure allows for the exploration of diverse configurations and parameter sets, enabling the study of the impact of intrinsic growth rates, transition rates, and cisplatin treatment on the population dynamics of ADRN, MES, and plastic cell phenotypes. The ensemble of simulations provides a comprehensive understanding of the observed experimental phenomena, including the enrichment of plastic subpopulations following cisplatin treatment of ADRN and MES cells.

Figure legends

Fig. 1: Phenotypic population dynamics are treatment-specific. a, SK-N-SH cells were FACS sorted based on CD44 expression level into three categories (low, intermediate and high) and cultured separately. The phenotypes of these sorted cells were assessed at 2, 5, and 12 days after the FACS sorting using Flow Cytometry. **b**, Stacked bar chart illustrating the percentage of cells in each CD44 expression category at different time points post-FACS sorting. Live cells were gated into $CD44^{low}$, $CD44^{int}$ and $CD44^{high}$ populations and plotted as the percentage. **c**, SK-N-SH cells FACS sorted as described above (**a**) were seeded at clonogenic density in 6 well plates and colony formation was assessed after 1 month using the Incucyte imaging. **d**, Box plot showing the number of colonies formed by cells in each CD44 FACS sorted population. Data are represented as mean ± standard deviation (SD) of biological replicates. Statistical significance is denoted using asterisks (*$P \leq 0.05$, **$P \leq 0.01$, ***$P \leq 0.001$). **e**, SK-N-SH cells were treated with compounds listed in Table 1, namely doxorubicin (0.107 uM), cisplatin (3.18uM), lorlatinib (10 uM), ruboxistaurin (15 uM), deferoxamine mesylate (DFO) (100uM), retinoic acid (RA) (2 uM), JQ1 (0.66 uM), tazemetostat (1 uM), IWP-2 (45.59 uM), XAV-939 (64.63 uM), CHIR99021 (5uM), TGFβI (10 uM) or rTGFβ (0.1 uM). IC_{50} concentrations were used for all compounds except for tazemetostat, DFO, RA, TGFbi and rTGFb for which a biologically active dose was used. Phenotypic changes were monitored on day 1, 2, 7, and 7 days after the removal of treatment by Flow Cytometry. Live cells were gated into $CD44^{low}$, $CD44^{int}$ and $CD44^{high}$ populations, and plotted as the percentage.

Fig. 2: Intrinsic determinism underlies persistence in neuroblastoma. a, SK-N-SH cells were barcoded with Cellecta barcodes in a lentiviral system and expanded. The population (referred to as POT) was divided into triplicates and from each of these, the cells were distributed equally into nine flasks. Among the nine replicates,

three were treated with IC_{50} doses of cisplatin, three were treated with IC_{50} doses of JQ1, and the remaining three replicates served as untreated controls. After 48 hrs of treatment, 10% of the cells from each replicate were collected and cryopreserved. The remaining cells in all replicates were re-seeded and left untreated for 10 days. After the 10-days untreated period, all cells were harvested and cryopreserved for further DNA and single-cell analysis. **b**, Shannon diversity index calculated per experimental condition visualised as a bar plot, colours indicate experimental condition. Statistical significance is denoted using asterisks (*P ≤ 0.05, **P ≤ 0.01, ***P ≤ 0.001) based on comparisons of ON to untreated, or dollar sign ($P ≤ 0.05, $$P ≤ 0.01, $$$P ≤ 0.001) based on comparisons of ON to OFF of the same treatment. Statistical significance of results was determined using pairwise t-tests and false discovery rate (FDR) < 0.05. **c**, Cumulative frequency distribution plots calculated per treatment group (lines coloured by treatment group), visualising cumulative barcode/clone ranked from most to least frequent. **d**, Clonal frequencies of 75 most highly abundant clones within POT were estimated based on the number of cells used for the DNA sequencing library preparation combined with barcode frequency. This was then visualized using a dot plot, where size reflects estimated frequency of each barcode (upper panel). Zoom in of a selection of clones to better visualise clonal dynamics between experimental conditions (bottom panel). **e**, Estimated clone frequency of clones in previous panel (bottom panel) through each experimental condition arm to visualise clonal dynamics. Lines represent each individual experimental replicate.

Fig. 3: Plasticity and selective cell state killing coordinate drug tolerance, persistence, and regrowth. a, UMAP plot of single cells from the scRNA-seq experiment, coloured by cell cluster. **b**, UMAP plots visualising cellular cluster, divided by treatment groups. **c,** UMAP plot of single cells from scRNA-seq experiment, coloured by AMT state. **d**, UMAP plots visualising AMT states divided by treatment group. **e**, Bar plot visualising the fold change of each AMT state divided by treatment group compared to untreated. Statistical significance is denoted using asterisks (*P ≤ 0.05, **P ≤ 0.01, ***P ≤ 0.001) based on comparing the results to the untreated control, or dollar sign ($P ≤ 0.05, $$P ≤ 0.01, $$$P ≤ 0.001) based on comparisons of ON to OFF of the same treatment. Statistical significance of results was determined using pairwise t-tests and false discovery rate (FDR) < 0.05. **f**, SK-N-SH cells were FACS sorted based on CD44 expression and treated with IC_{50} concentrations of either Cisplatin or JQ1 for 7 days. Following the removal of treatment, CD44 expression was evaluated by Flow Cytometry at 7 days and 1 month. **g**, Box plots represent the $CD44^{low}$ and $CD44^{high}$ expression levels expressed as fold change relative to the UT samples. Live cells were gated into $CD44^{low}$ and $CD44^{high}$ populations and data are represented as mean ± standard deviation (SD) of biological replicates. Statistical significance is denoted using asterisks (*P ≤ 0.05, **P ≤ 0.01, ***P ≤ 0.001) based on t-test comparing the results to the untreated control.

Fig. 4: **Cell state alone does not solely determine clonal dominance. a**, Schematic representation of the analysis conducted on DTP cells. DTPs were initially plotted on the UMAP space in the OFF experimental condition. The same clones were then re-plotted in the untreated condition to visualize their origins pre-treatment across cell clusters. **b-e** UMAP plots divided by treatment group, specifically representing the DTP clones pre (right plots) and post treatment **(**left plots) and color-coded by cell cluster. Bar plot summarising AMT state proportion of DTP clones pre and post treatment. **f.** Alluvial diagrams representing cell state transitions between untreated experimental conditions. **g.** Untreated and cisplatin ON (left panel) and cisplatin

ON and cisplatin OFF (right panel). **h.** Untreated and JQ1 ON (left panel) and JQ1 ON and JQ1 OFF (right panel). Bar coloured by AMT state of clone, flow parameters colour-coded by phenotypic transition. **h**, Graphical illustration of cisplatin-treatment on neuroblastoma cells. DTP-entry is mediated by both ADRN preferential cell killing and in small measure by ADRN-to-MES transitions. The resulting MES-enriched cells regrow and fully recover from treatment by undergoing MES-to-ADRN transitions.

Fig. 5: Adrenergic to mesenchymal transitions are drug-specific. a. Trajectory plots of three treatment-specific lineages (cisplatin-, cisplatin OFF-, and JQ1-specific), coloured by annotated functional cluster. **b, c, d.** Dynamical manifolds representing cell state landscapes in neuroblastoma for different treatment conditions: (**b**) untreated, (**c**) cisplatin-treated, (**d**) JQ1-treated. Cells are coloured by MuTrans attractor wells. Attractor wells are labelled from 1 to *N*, denoting their relative energy ranking, which also relates to attractor well depth from deepest to shallowest. **e, f, g**. The global lineage structure inferred by MuTrans Maximum Probability Flow Tree (MPFT) algorithm, overlaid on the dynamical manifold for each of the three treatment conditions: (**e**) untreated, (**f**) cisplatin-treated, (**g**) JQ1-treated**.** Cells are coloured by MuTrans attractor wells. Greyness indicates energy values of the dynamical manifold, with darker colours representing more negative energy values (greater depth). **h, i, j.** The transition path analysis using the MuTrans Most Probable Path Tree (MPPT) approach for ADRN to MES transitions, overlaid on the dynamical manifold for each of the three treatment conditions: (**h**) untreated, (**i**) cisplatin-treated, (**j**) JQ1-treated. The MPPTs represent transition routes from a start to an end state, which in this case are wells that feature at the end of branches in the global lineage structure (**e, f, g**). Transition routes can pass through attractor wells other than the root and end state, which act as intermediate nodes in transition. Numbers indicate the relative likelihood of each transition path. Cells are coloured by MuTrans attractor wells. Greyness indicates energy values of the dynamical manifold, with darker colours representing more negative energy values (greater depth).

Fig. 6: Plasticity is a heterogeneous and heritable dynamic trait. a, Schematic representation of the experimental design and possible experimental outcomes to determine the heritability of plasticity traits. SK-N-SH cells were sorted by FACS into ADRN ($CD44^{low}$) and MES ($CD44^{high}$) populations. Single cell clones were generated using limited dilution approaches and the phenotypic composition of clones were determined by flow cytometry. **b**, Stacked bar chart displaying the phenotypic composition of single cell clones after approximately 10 weeks in culture, determined by flow cytometry. Live cells were gated into $CD44^{low}$, $CD44^{int}$ and $CD44^{high}$ populations, and plotted as the percentage of $CD44^{low}$ and $CD44^{high}$ (y axis) for each single cell clone (x axis). Clones were named A-R based on the percentage $CD44^{high}$ on this first analysis. **c**, Schematic representation of the reaction norms experimental design (left) and graphical outcomes for plasticity traits (right). G1 and G2 refer to alternative heritable traits. **d**, Reaction norms graphs for parental SK-N-SH cells, and single cell-derived clones. Cells were analysed by flow cytometry immediately after cisplatin treatment (day 0; environment 1) and after 14 days recovery (day 14; environment 2). Live cells were gated into $CD44^{low}$, $CD44^{int}$ and $CD44^{high}$ populations, and plotted as the percentage of $CD44^{low}$ and $CD44^{high}$ (y axis) at each time point (x axis). Two replicates were analysed per time point.

Fig. 7: Plasticity systems are subject to evolutionary dynamics. a, Bar charts displaying area under the curve (AUC) values of the cisplatin dose response curves (left), response to a fixed concentration (3.18 uM) of cisplatin (middle) and growth over 7 days (right). Bars display single cell-derived clones and parental SK-N-SH cultures. Bars are ordered by the slope of the reaction norms graph, which is indicative of plasticity capacity. Error bars display +/- standard deviation of replicate wells. **b**, Cell population model showing the transitions, growth and death rates of the different cell phenotypes. The plastic cell phenotypes are denoted by *. **c**, Density distribution of the final population size as a function of the total carrying capacity of the population. The red distribution denotes the population with the drug, cisplatin and the black distribution denotes the population without. **d**, Scatterplot showing the fraction of mesenchymal cell population in comparison to the total carrying capacity between the cisplatin treated and cisplatin untreated conditions. The red line indicates equal fractions of mesenchymal phenotypes both before and after the treatment. **e**, Density plots of mesenchymal fractions in parameter sets that enrich for mesenchymal fraction after treatment with cisplatin. **f**, Density plots of adrenergic fraction in parameter sets that enrich for mesenchymal fraction after treatment with cisplatin. **g**, Density plots of fraction of plastic cell phenotypes in parameter sets that enrich for mesenchymal fraction after treatment with cisplatin. **h,** Conceptual model by which cisplatin treatment enriches for dynamic plasticity systems.

Acknowledgements

We thank Katerina Rekopoulou and Nik Matthews for assistance with sample and library preparation for single-cell RNA-sequencing; Jan Molenaar for providing the patient-derived spheroid lines; Andrea Sottariva for sharing the Cellecta barcode library and expertise in barcoding the cells as well as Salvatore Milite and Haider Tari for assistance and technical advice in analysis and barcode sequencing processing; Yura Grabovska and Chris Jones for technical expertise in the analysis of scRNA-seq data; Melanie Beckett, Elizabeth R. Tucker, Evon Poon and Karen Barker for helpful discussion and technical advice; Peijie Zhou for help with the MuTrans analysis; Oscar M. Rueda and Maurizio Callari for technical advice regarding WGS and WES analyses. We also acknowledge the ICR facilities: Light Microscopy and Confocal, Flow Cytometry and Genomics. A.B. is supported by ICR London. This study was supported by Little Princess Trust Innovation Grant LPTINS2\9 (to A.B and L.C).

Author contributions

Methodology, C.R., S.H., A.S., E.C., C.E., A.S.S., S.S., A.A.A., H.C., M.D.M.; experimental design, C.R., S.H., A.S., M.D.M., A.B.; experimental investigation, C.R., S.H., A.S., C.E., A.A.A.; analytical investigation, S.H., E.C., A.S.S., S.S., M.D.M.; writing–original draft, C.R., A.B.; writing–review and editing, C.R., S.H., A.S., E.C., C.E., S.S., M.K.J., M.D.M., A.B.; resources, L.C.; conceptualization, A.B.; project administration, A.B.; funding acquisition, L.C., A.B.

References

1. DuBois, S. G., Macy, M. E. & Henderson, T. O. High-Risk and Relapsed Neuroblastoma: Toward More Cures and Better Outcomes. *American Society of Clinical Oncology Educational Book* 768–780 (2022) doi:10.1200/EDBK_349783.

2. Gröbner, S. N. *et al.* The landscape of genomic alterations across childhood cancers. *Nature* **555**, 321–327 (2018).
3. Kandoth, C. *et al.* Mutational landscape and significance across 12 major cancer types. *Nature* **502**, 333–339 (2013).
4. Filbin, M. & Monje, M. Developmental origins and emerging therapeutic opportunities for childhood cancer. *Nat Med* **25**, 367–376 (2019).
5. Pugh, T. J. *et al.* The genetic landscape of high-risk neuroblastoma. *Nat Genet* **45**, 279–284 (2013).
6. Bosse, K. R. & Maris, J. M. Advances in the translational genomics of neuroblastoma: From improving risk stratification and revealing novel biology to identifying actionable genomic alterations: Advances in Neuroblastoma Genomics. *Cancer* **122**, 20–33 (2016).
7. Schramm, A. *et al.* Mutational dynamics between primary and relapse neuroblastomas. *Nat Genet* **47**, 872–877 (2015).
8. Nakagawara, A. *et al.* Neuroblastoma. *JJCO* **48**, 214–241 (2018).
9. Gundem, G. *et al.* Clonal evolution during metastatic spread in high-risk neuroblastoma. *Nat Genet* **55**, 1022–1033 (2023).
10. Bedoya-Reina, O. C. *et al.* Single-nuclei transcriptomes from human adrenal gland reveal distinct cellular identities of low and high-risk neuroblastoma tumors. *Nat Commun* **12**, 5309 (2021).
11. Dong, R. *et al.* Single-Cell Characterization of Malignant Phenotypes and Developmental Trajectories of Adrenal Neuroblastoma. *Cancer Cell* **38**, 716-733.e6 (2020).
12. Jansky, S. *et al.* Single-cell transcriptomic analyses provide insights into the developmental origins of neuroblastoma. *Nat Genet* **53**, 683–693 (2021).
13. Kameneva, P. *et al.* Single-cell transcriptomics of human embryos identifies multiple sympathoblast lineages with potential implications for neuroblastoma origin. *Nat Genet* **53**, 694–706 (2021).
14. Kildisiute, G. *et al.* Tumor to normal single-cell mRNA comparisons reveal a pan-neuroblastoma cancer cell. *Sci Adv* **7**, eabd3311 (2021).
15. Olsen, T. K. *et al.* Malignant Schwann cell precursors mediate intratumoral plasticity in human neuroblastoma. *bioRxiv* (2020) doi:10.1101/2020.05.04.077057.
16. Chapple, R. H. *et al.* An unsupervised learning approach uncovers divergent mesenchymal-like gene expression programs across human neuroblastoma tumors, preclinical models, and chemotherapy-exposed tumors. *bioRxiv* (2023) doi:10.1101/2023.04.13.536639.

17. Boeva, V. *et al.* Heterogeneity of neuroblastoma cell identity defined by transcriptional circuitries. *Nat Genet* **49**, 1408–1413 (2017).

18. van Groningen, T. *et al.* Neuroblastoma is composed of two super-enhancer-associated differentiation states. *Nat Genet* **49**, 1261–1266 (2017).

19. Thirant, C. *et al.* Reversible transitions between noradrenergic and mesenchymal tumor identities define cell plasticity in neuroblastoma. *Nat Commun* **14**, 2575 (2023).

20. Yuan, X. *et al.* Single-cell profiling of peripheral neuroblastic tumors identifies an aggressive transitional state that bridges an adrenergic-mesenchymal trajectory. *Cell Reports* **41**, 111455 (2022).

21. Fetahu, I. S. *et al.* Single-cell transcriptomics and epigenomics unravel the role of monocytes in neuroblastoma bone marrow metastasis. *Nat Commun* **14**, 3620 (2023).

22. Sharma, S. V. *et al.* A Chromatin-Mediated Reversible Drug-Tolerant State in Cancer Cell Subpopulations. *Cell* **141**, 69–80 (2010).

23. Pu, Y. *et al.* Drug-tolerant persister cells in cancer: the cutting edges and future directions. *Nat Rev Clin Oncol* **20**, 799–813 (2023).

24. Dhanyamraju, P. K., Schell, T. D., Amin, S. & Robertson, G. P. Drug-Tolerant Persister Cells in Cancer Therapy Resistance. *Cancer Res* **82**, 2503–2514 (2022).

25. van Groningen, T. *et al.* A NOTCH feed-forward loop drives reprogramming from adrenergic to mesenchymal state in neuroblastoma. *Nat Commun* **10**, 1530 (2019).

26. Ross, R. A. *et al.* Human neuroblastoma I-type cells are malignant neural crest stem cells. *Cell Growth Differ* **6**, 449–456 (1995).

27. Shannon, C. E. A Mathematical Theory of Communication. *Bell System Technical Journal* **27**, 379–423 (1948).

28. Chae, Y. K. *et al.* Epithelial-mesenchymal transition (EMT) signature is inversely associated with T-cell infiltration in non-small cell lung cancer (NSCLC). *Sci Rep* **8**, 2918 (2018).

29. Tan, T. Z. *et al.* Epithelial□mesenchymal transition spectrum quantification and its efficacy in deciphering survival and drug responses of cancer patients. *EMBO Mol Med* **6**, 1279–1293 (2014).

30. Wellens, L. M. *et al.* Anti-GD2-IRDye800CW as a targeted probe for fluorescence-guided surgery in neuroblastoma. *Sci Rep* **10**, 17667 (2020).

31. Whiting, F. J. H., Household, J., Baker, A.-M., Sottoriva, A. & Graham, T. A. Phenotypic noise and plasticity in cancer evolution. *Trends in Cell Biology* S0962892423002064 (2023) doi:10.1016/j.tcb.2023.10.002.

32. Street, K. *et al.* Slingshot: cell lineage and pseudotime inference for single-cell transcriptomics. *BMC Genomics* **19**, 477 (2018).

33. Zhou, P., Wang, S., Li, T. & Nie, Q. Dissecting transition cells from single-cell transcriptome data through multiscale stochastic dynamics. *Nat Commun* **12**, 5609 (2021).

34. Luria, S. E. & Delbrück, M. Mutations of Bacteria from Virus Sensitivity to Virus Resistance. *Genetics* **28**, 491–511 (1943).

35. Gomulkiewicz, R. & Kirkpatrick, M. Quantitative Genetics and the Evolution of Reaction Norms. *Evolution* **46**, 390 (1992).

36. Gomulkiewicz, R. & Stinchcombe, J. R. Phenotypic plasticity made simple, but not too simple. *American J of Botany* **109**, 1519–1524 (2022).

37. Ng, E. T. H. & Kinjo, A. R. Plasticity-led evolution as an intrinsic property of developmental gene regulatory networks. *Sci Rep* **13**, 19830 (2023).

38. Levis, N. A. & Pfennig, D. W. Evaluating 'Plasticity-First' Evolution in Nature: Key Criteria and Empirical Approaches. *Trends in Ecology & Evolution* **31**, 563–574 (2016).

39. Griffiths, J. A., Richard, A. C., Bach, K., Lun, A. T. L. & Marioni, J. C. Detection and removal of barcode swapping in single-cell RNA-seq data. *Nat Commun* **9**, 2667 (2018).

40. Shaffer, S. M. *et al.* Rare cell variability and drug-induced reprogramming as a mode of cancer drug resistance. *Nature* **546**, 431–435 (2017).

41. Shaffer, S. M. *et al.* Memory Sequencing Reveals Heritable Single-Cell Gene Expression Programs Associated with Distinct Cellular Behaviors. *Cell* **182**, 947-959.e17 (2020).

42. Woltereck, L. Weitere experimentelle Untersuchungen uber Artveranderung, speziell uberdas Wesen quantitativer Artunterschyiede bei Daphniden. *Verh. D. Tsch. Zool. Ges* **19**, 110–173 (1909).

43. Johannsen, W. The genotype conception of heredity. *American Naturalist* **45**, 129–159 (1911).

44. Schmalhausen, I. I. Factors of evolution: the theory of stabilizing selection. *University of Chicago Press, Chicago, Illinois, USA.* (1949).

45. Bruna, A. *et al.* A Biobank of Breast Cancer Explants with Preserved Intra-tumor Heterogeneity to Screen Anticancer Compounds. *Cell* **167**, 260-274.e22 (2016).

46. Li, H. & Durbin, R. Fast and accurate short read alignment with Burrows–Wheeler transform. *Bioinformatics* **25**, 1754–1760 (2009).

47. Danecek, P. *et al.* Twelve years of SAMtools and BCFtools. *GigaScience* **10**, giab008 (2021).

48. Lun, A. T. L. *et al.* EmptyDrops: distinguishing cells from empty droplets in droplet-based single-cell RNA sequencing data. *Genome Biol* **20**, 63 (2019).

49. McCarthy, D. J., Campbell, K. R., Lun, A. T. L. & Wills, Q. F. Scater: pre-processing, quality control, normalization and visualization of single-cell RNA-seq data in R. *Bioinformatics* **33**, 1179–1186 (2017).

50. Satija, R., Farrell, J. A., Gennert, D., Schier, A. F. & Regev, A. Spatial reconstruction of single-cell gene expression data. *Nat Biotechnol* **33**, 495–502 (2015).

51. Wu, T. *et al.* clusterProfiler 4.0: A universal enrichment tool for interpreting omics data. *The Innovation* **2**, 100141 (2021).

52. Yu, G., Wang, L.-G., Han, Y. & He, Q.-Y. clusterProfiler: an R Package for Comparing Biological Themes Among Gene Clusters. *OMICS: A Journal of Integrative Biology* **16**, 284–287 (2012).

53. Wolf, F. A., Angerer, P. & Theis, F. J. SCANPY: large-scale single-cell gene expression data analysis. *Genome Biol* **19**, 15 (2018).

54. Andrews, S. A quality control tool for high throughput sequence data. Available online at: https://www.bioinformatics.babraham.ac.uk/projects/fastqc/. *Babraham Institute* (2010).

55. Dobin, A. *et al.* STAR: ultrafast universal RNA-seq aligner. *Bioinformatics* **29**, 15–21 (2013).

56. Anders, S., Pyl, P. T. & Huber, W. HTSeq—a Python framework to work with high-throughput sequencing data. *Bioinformatics* **31**, 166–169 (2015).

57. Love, M. I., Huber, W. & Anders, S. Moderated estimation of fold change and dispersion for RNA-seq data with DESeq2. *Genome Biol* **15**, 550 (2014).

58. McKenna, A. *et al.* The Genome Analysis Toolkit: A MapReduce framework for analyzing next-generation DNA sequencing data. *Genome Res.* **20**, 1297–1303 (2010).

59. Cibulskis, K. *et al.* Sensitive detection of somatic point mutations in impure and heterogeneous cancer samples. *Nat Biotechnol* **31**, 213–219 (2013).

60. Scheinin, I. *et al.* DNA copy number analysis of fresh and formalin-fixed specimens by shallow whole-genome sequencing with identification and exclusion of problematic regions in the genome assembly. *Genome Res.* **24**, 2022–2032 (2014).

Figure 1

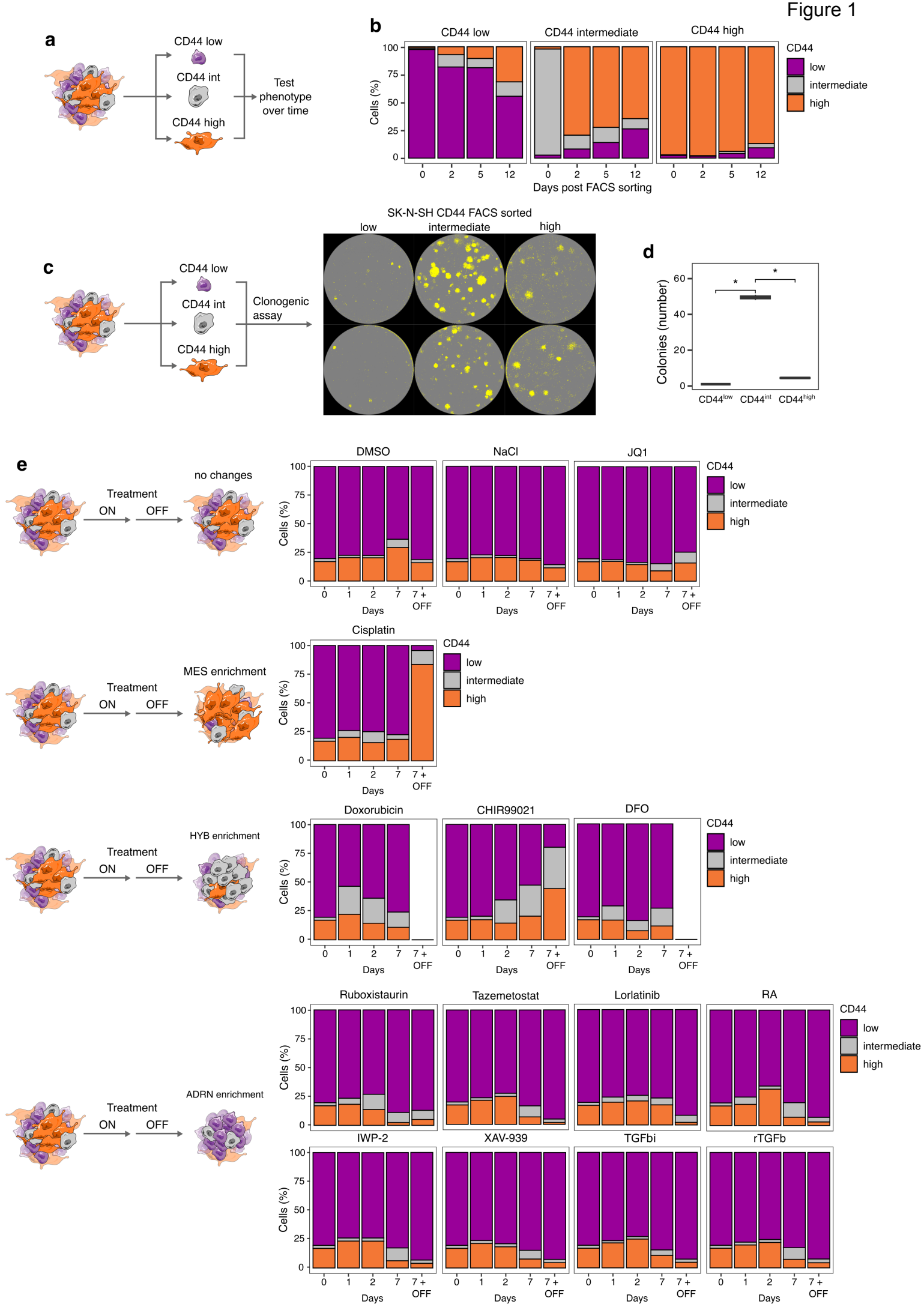
a
CD44 low
CD44 int
CD44 high
Test phenotype over time
b
CD44 low
CD44 intermediate
CD44 high
Cells (%)
Days post FACS sorting
CD44
low
intermediate
high
c
CD44 low
CD44 int
CD44 high
Clonogenic assay
SK-N-SH CD44 FACS sorted
low
intermediate
high
d
Colonies (number)
CD44low
CD44int
CD44high
e
Treatment
ON
OFF
no changes
DMSO
NaCl
JQ1
Days
Cisplatin
MES enrichment
HYB enrichment
Doxorubicin
CHIR99021
DFO
ADRN enrichment
Ruboxistaurin
Tazemetostat
Lorlatinib
RA
IWP-2
XAV-939
TGFbi
rTGFb

Figure 2

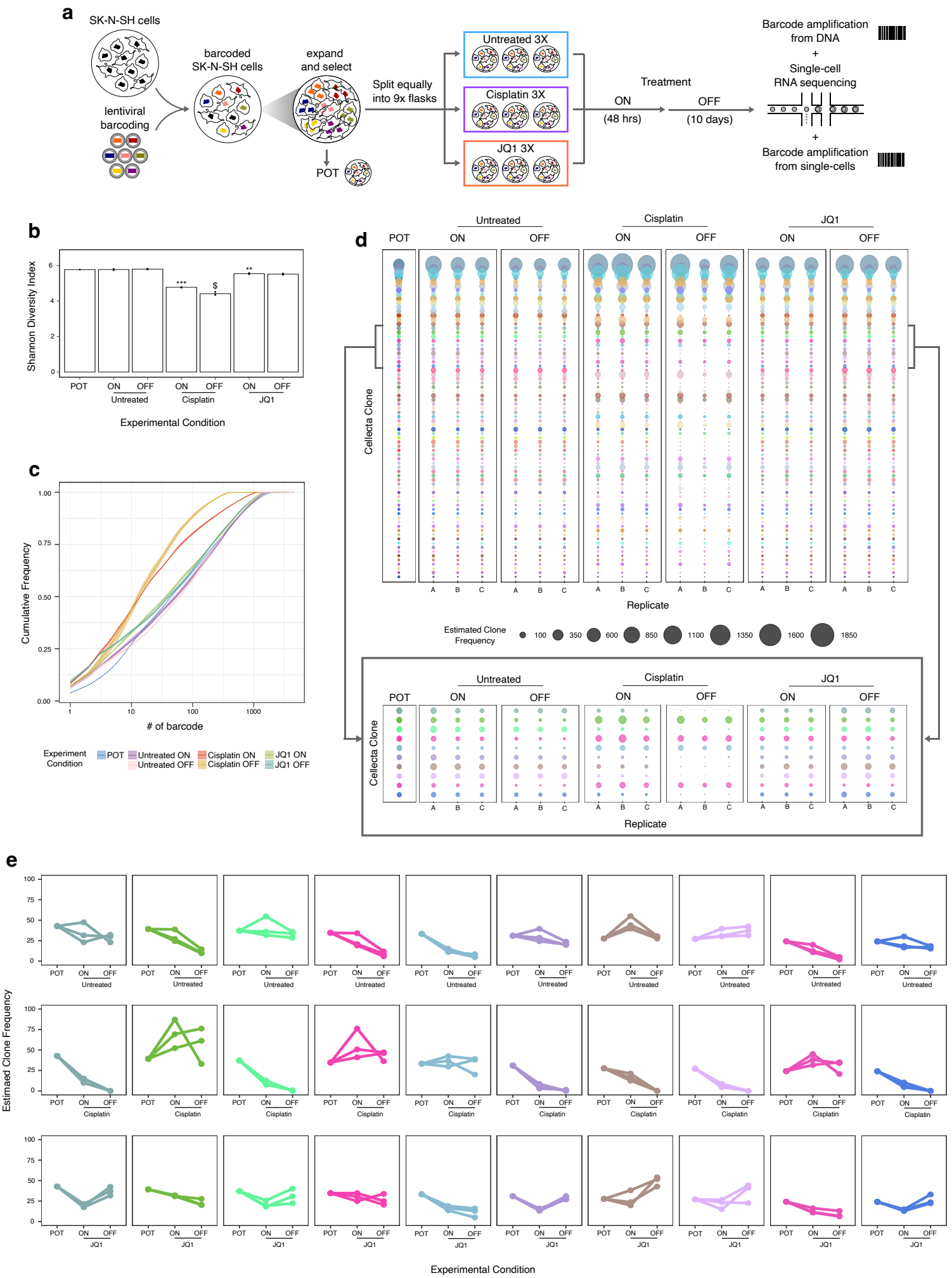
a
SK-N-SH cells
lentiviral barcoding
barcoded SK-N-SH cells
expand and select
POT
Split equally into 9x flasks
Untreated 3X
Cisplatin 3X
JQ1 3X
Treatment
ON (48 hrs)
OFF (10 days)
Barcode amplification from DNA
+
Single-cell RNA sequencing
+
Barcode amplification from single-cells
b
Shannon Diversity Index
POT
ON
OFF
Untreated
Cisplatin
JQ1
Experimental Condition
c
Cumulative Frequency
# of barcode
Experiment Condition
POT
Untreated ON
Untreated OFF
Cisplatin ON
Cisplatin OFF
JQ1 ON
JQ1 OFF
d
Cellecta Clone
Replicate
Estimated Clone Frequency
100
350
600
850
1100
1350
1600
1850
e
Estimaed Clone Frequency
Experimental Condition

Figure 3

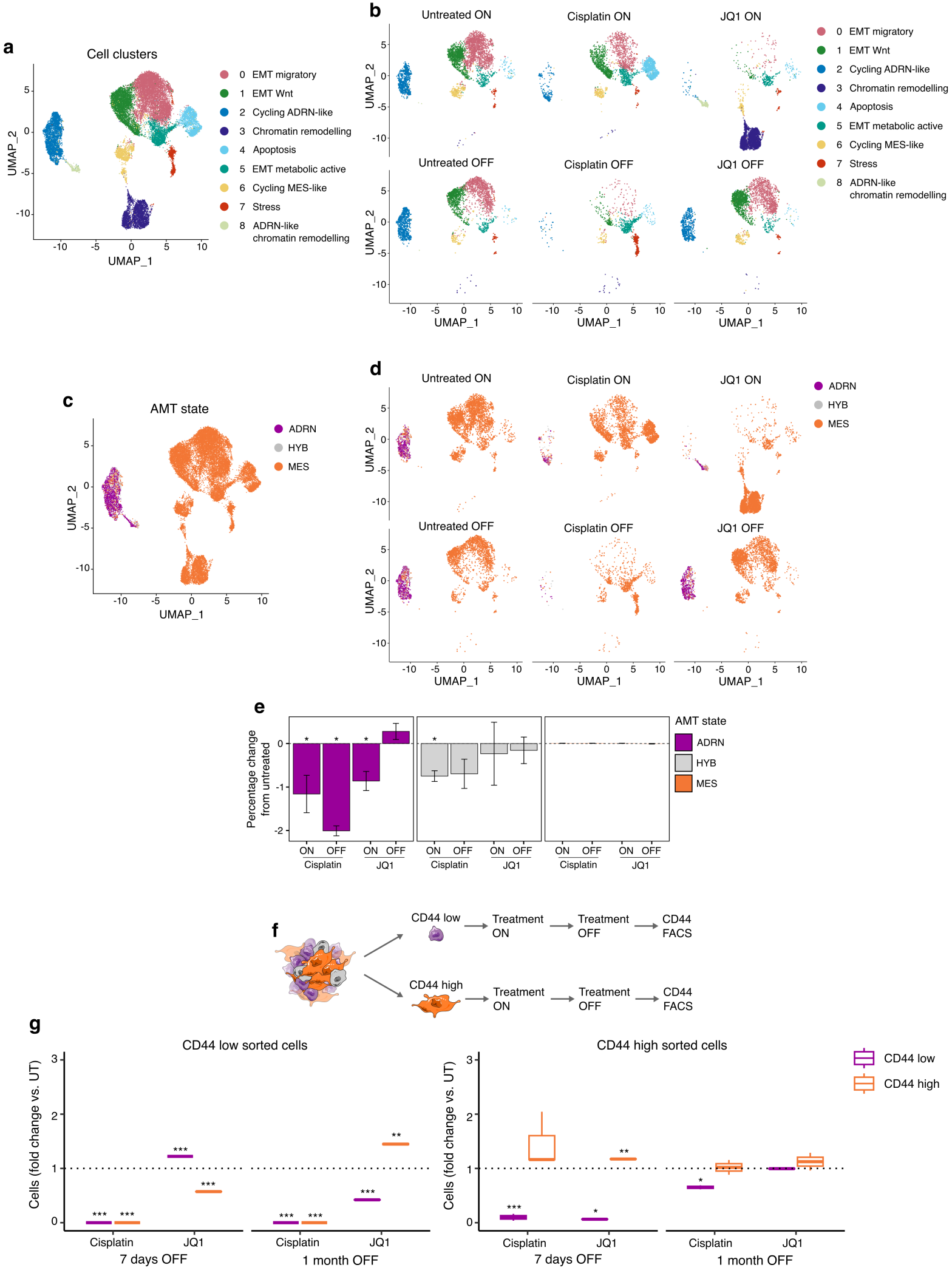
a
Cell clusters
UMAP_2
UMAP_1
0 EMT migratory
1 EMT Wnt
2 Cycling ADRN-like
3 Chromatin remodelling
4 Apoptosis
5 EMT metabolic active
6 Cycling MES-like
7 Stress
8 ADRN-like chromatin remodelling
b
Untreated ON
Cisplatin ON
JQ1 ON
Untreated OFF
Cisplatin OFF
JQ1 OFF
c
AMT state
ADRN
HYB
MES
d
e
Percentage change from untreated
ON OFF ON OFF
Cisplatin JQ1
f
CD44 low
CD44 high
Treatment ON
Treatment OFF
CD44 FACS
g
CD44 low sorted cells
CD44 high sorted cells
Cells (fold change vs. UT)
Cisplatin
JQ1
7 days OFF
1 month OFF

Figure 4

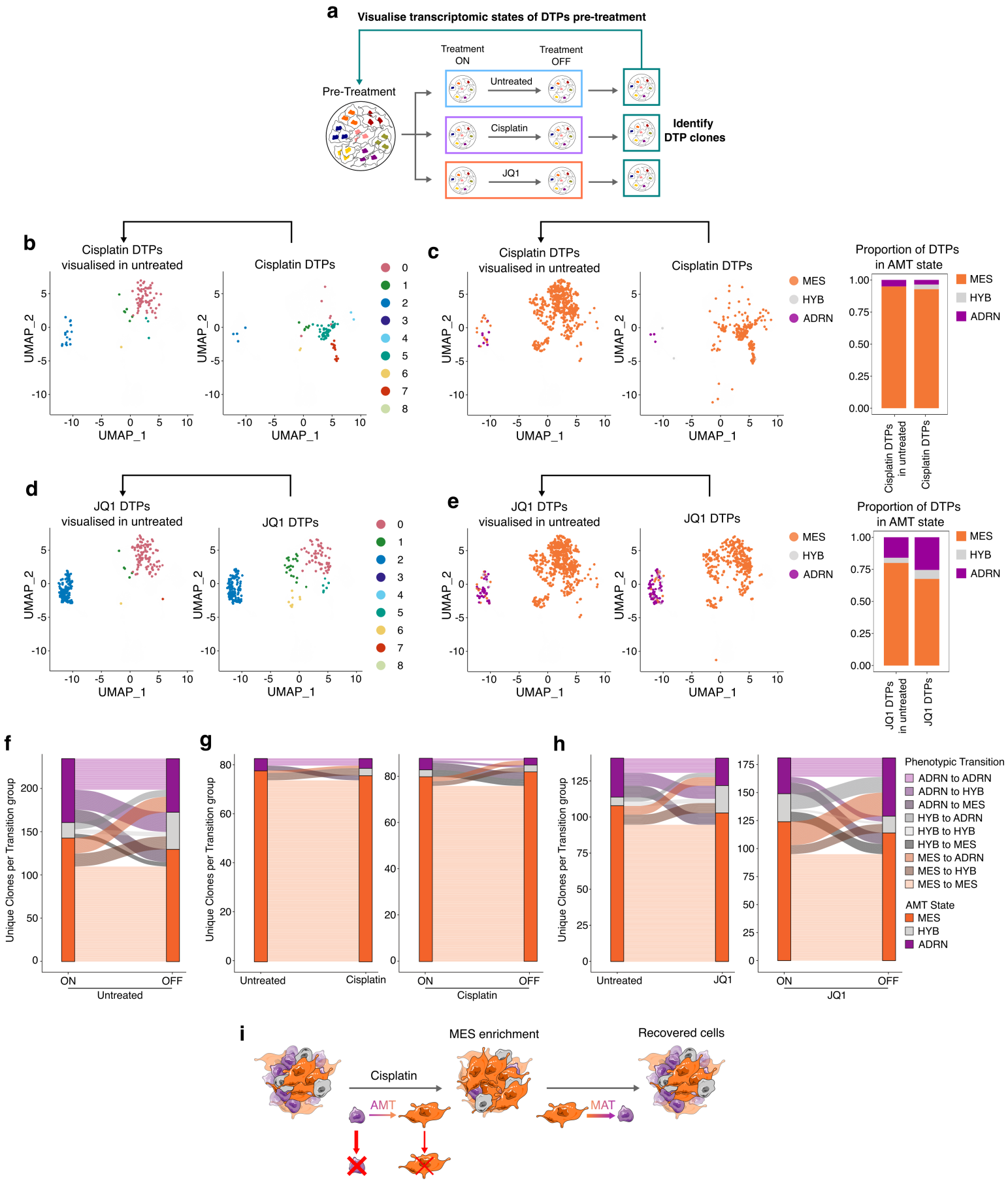
a
Visualise transcriptomic states of DTPs pre-treatment
Pre-Treatment
Treatment ON
Treatment OFF
Untreated
Cisplatin
JQ1
Identify DTP clones
b
Cisplatin DTPs visualised in untreated
Cisplatin DTPs
UMAP_1
UMAP_2
c
Proportion of DTPs in AMT state
MES
HYB
ADRN
Cisplatin DTPs in untreated
Cisplatin DTPs
d
JQ1 DTPs visualised in untreated
JQ1 DTPs
e
JQ1 DTPs in untreated
JQ1 DTPs
f
Unique Clones per Transition group
ON
OFF
Untreated
g
Cisplatin
h
JQ1
Phenotypic Transition
ADRN to ADRN
ADRN to HYB
ADRN to MES
HYB to ADRN
HYB to HYB
HYB to MES
MES to ADRN
MES to HYB
MES to MES
AMT State
i
MES enrichment
Recovered cells
AMT
MAT

Figure 5

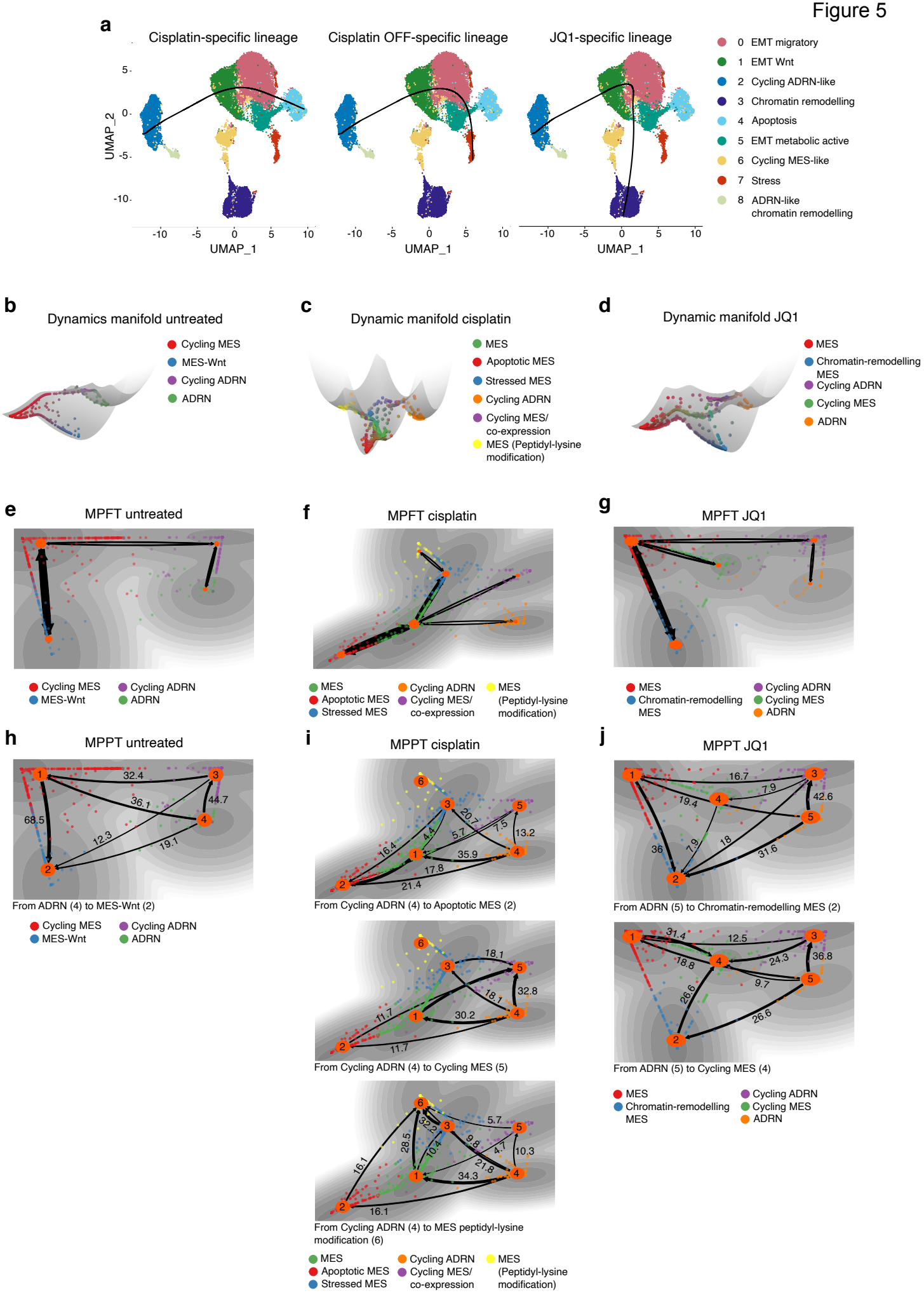
a
Cisplatin-specific lineage
Cisplatin OFF-specific lineage
JQ1-specific lineage
UMAP_2
UMAP_1
0 EMT migratory
1 EMT Wnt
2 Cycling ADRN-like
3 Chromatin remodelling
4 Apoptosis
5 EMT metabolic active
6 Cycling MES-like
7 Stress
8 ADRN-like chromatin remodelling
b
Dynamics manifold untreated
Cycling MES
MES-Wnt
Cycling ADRN
ADRN
c
Dynamic manifold cisplatin
MES
Apoptotic MES
Stressed MES
Cycling ADRN
Cycling MES/ co-expression
MES (Peptidyl-lysine modification)
d
Dynamic manifold JQ1
MES
Chromatin-remodelling MES
Cycling ADRN
Cycling MES
ADRN
e
MPFT untreated
Cycling MES
MES-Wnt
Cycling ADRN
ADRN
f
MPFT cisplatin
MES
Apoptotic MES
Stressed MES
Cycling ADRN
Cycling MES/ co-expression
MES (Peptidyl-lysine modification)
g
MPFT JQ1
MES
Chromatin-remodelling MES
Cycling ADRN
Cycling MES
ADRN
h
MPPT untreated
From ADRN (4) to MES-Wnt (2)
Cycling MES
MES-Wnt
Cycling ADRN
ADRN
i
MPPT cisplatin
From Cycling ADRN (4) to Apoptotic MES (2)
From Cycling ADRN (4) to Cycling MES (5)
From Cycling ADRN (4) to MES peptidyl-lysine modification (6)
MES
Apoptotic MES
Stressed MES
Cycling ADRN
Cycling MES/ co-expression
MES (Peptidyl-lysine modification)
j
MPPT JQ1
From ADRN (5) to Chromatin-remodelling MES (2)
From ADRN (5) to Cycling MES (4)
MES
Chromatin-remodelling MES
Cycling ADRN
Cycling MES
ADRN

Figure 6

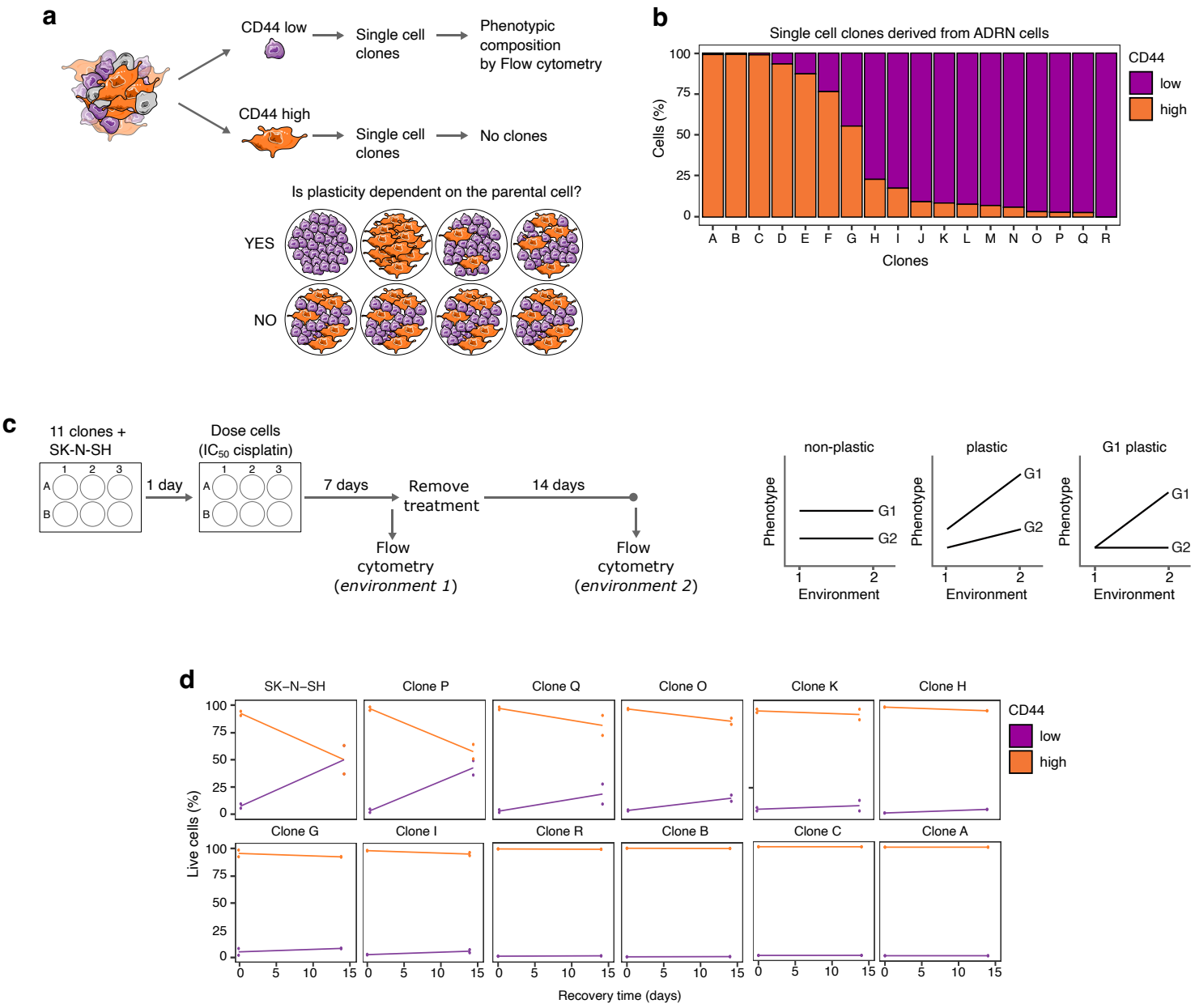
a
CD44 low
Single cell clones
Phenotypic composition by Flow cytometry
CD44 high
Single cell clones
No clones
Is plasticity dependent on the parental cell?
YES
NO
b
Single cell clones derived from ADRN cells
Cells (%)
100
75
50
25
0
A B C D E F G H I J K L M N O P Q R
Clones
CD44
low
high
c
11 clones + SK-N-SH
1 2 3
A
B
1 day
Dose cells (IC_{50} cisplatin)
7 days
Remove treatment
14 days
Flow cytometry (environment 1)
Flow cytometry (environment 2)
non-plastic
plastic
G1 plastic
Phenotype
G1
G2
1
2
Environment
d
SK–N–SH
Clone P
Clone Q
Clone O
Clone K
Clone H
Clone G
Clone I
Clone R
Clone B
Clone C
Clone A
Live cells (%)
100
75
50
25
0
0 5 10 15
Recovery time (days)
CD44
low
high

Figure 7

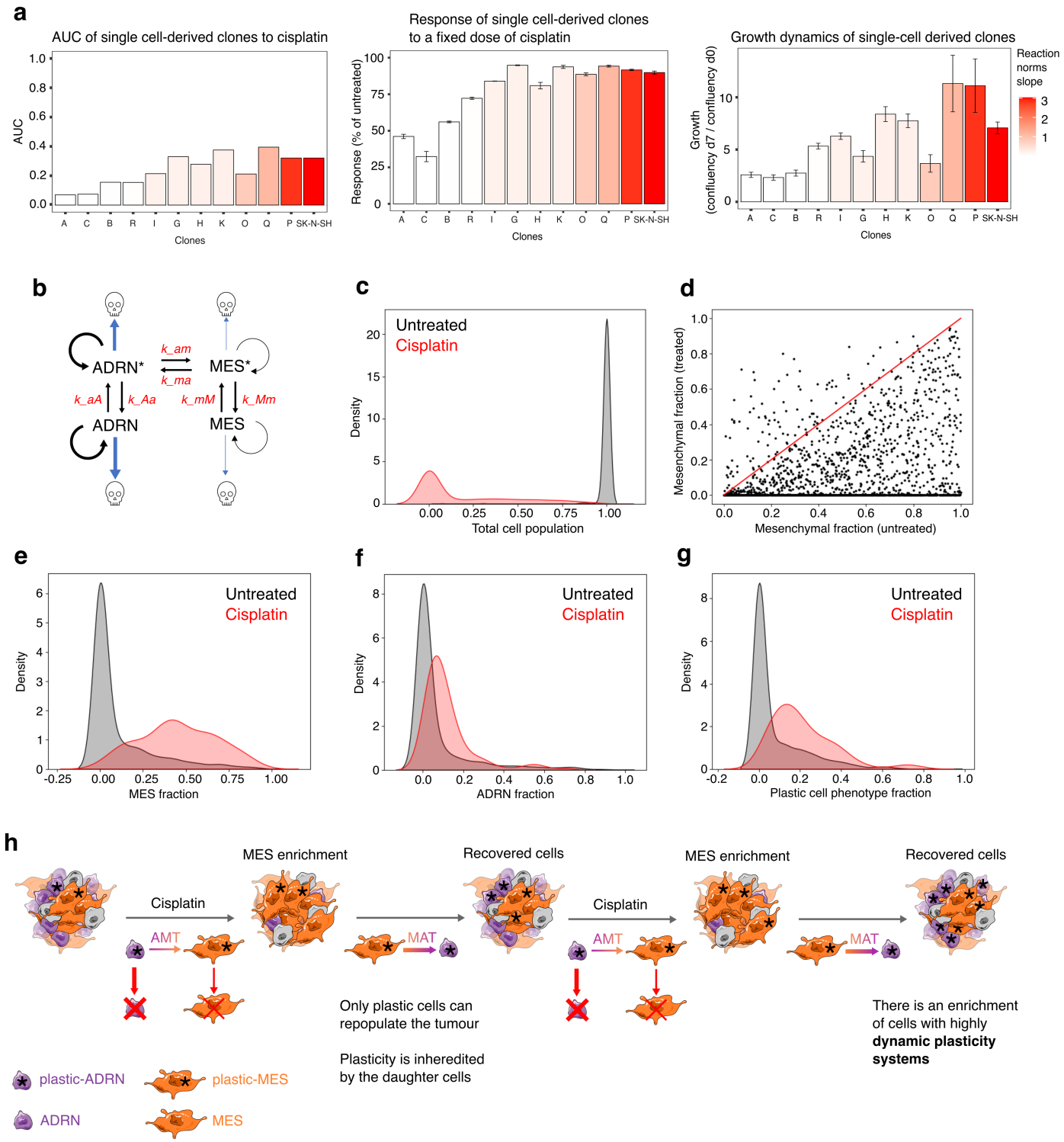
a
AUC of single cell-derived clones to cisplatin
AUC
Clones
Response of single cell-derived clones to a fixed dose of cisplatin
Response (% of untreated)
Growth dynamics of single-cell derived clones
Growth (confluency d7 / confluency d0)
Reaction norms slope
A C B R I G H K O Q P SK-N-SH
b
ADRN*
MES*
ADRN
MES
k_am
k_ma
k_aA
k_Aa
k_mM
k_Mm
c
Untreated
Cisplatin
Density
Total cell population
d
Mesenchymal fraction (treated)
Mesenchymal fraction (untreated)
e
MES fraction
f
ADRN fraction
g
Plastic cell phenotype fraction

h
MES enrichment
Recovered cells
Cisplatin
AMT
MAT
Only plastic cells can repopulate the tumour
Plasticity is inheredited by the daughter cells
There is an enrichment of cells with highly **dynamic plasticity systems**
plastic-ADRN
plastic-MES
ADRN
MES